InSight Pressure Data Recalibration, and its Application to the Study of Long-Term Pressure Changes on Mars

L.Lange[1], F.Forget[1], D.Banfield[2], M.Wolff[3], A.Spiga[1,4], E.Millour[1], D. Viúdez-Moreiras[5], A.Bierjon[1], S.Piqueux[6], C.Newman[7], J.Pla-García[5,8], W.B.Banerdt[6]

[1]Laboratoire de Météorologie Dynamique,Institut Pierre-Simon Laplace (LMD/IPSL), Sorbonne Université, Centre National de la Recherche Scientifique (CNRS), École Polytechnique, École Normale Supérieure (ENS), Paris, France
[2]Cornell Center for Astrophysics and Planetary Science, Cornell University, Ithaca, NY, USA
[3]Space Science Institute, Boulder, CO, USA
[4]Institut Universitaire de France, Paris, France
[5]Centro de Astrobiología (CSIC-INTA) and National Institute for Aerospace Technology (INTA), Madrid, Spain
[6]Jet Propulsion Laboratory, California Institute of Technology, Pasadena, CA 91109, USA
[7]Aeolis Research, Unit 5, Chandler, AZ, USA
[8]Southwest Research Institute, Boulder, CO, USA

Key Points:

- We propose a recalibration of InSight pressure data to correct an unexpected sensitivity to the sensor temperature;
- A comparison between the InSight and Viking 1 pressure data does not show secular changes in the global mass of the atmosphere;
- This comparison also supports the absence of long-term variability in the dynamics of seasonal cap formation and sublimation.

Corresponding author: Lucas Lange, `lucas.lange@lmd.ipsl.fr`

24 **Abstract**

25   Observations of the South Polar Residual Cap suggest a possible erosion of the cap,
26 leading to an increase of the global mass of the atmosphere. We test this assumption by
27 making the first comparison between Viking 1 and InSight surface pressure data, which
28 were recorded 40 years apart. Such a comparison also allows us to determine changes
29 in the dynamics of the seasonal ice caps between these two periods. To do so, we first
30 had to recalibrate the InSight pressure data because of their unexpected sensitivity to
31 the sensor temperature. Then, we had to design a procedure to compare distant pres-
32 sure measurements. We propose two surface pressure interpolation methods at the lo-
33 cal and global scale to do the comparison. The comparison of Viking and InSight sea-
34 sonal surface pressure variations does not show major changes in the CO_2 cycle. Such
35 conclusions are also supported by an analysis of Mars Science Laboratory (MSL) pres-
36 sure data. Further comparisons with images of the south seasonal cap taken by the Viking
37 2 orbiter and MARCI camera do not display significant changes in the dynamics of this
38 cap over a 40 year period. Only a possible larger extension of the North Cap after the
39 global storm of MY 34 is observed, but the physical mechanisms behind this anomaly
40 are not well determined. Finally, the first comparison of MSL and InSight pressure data
41 suggests a pressure deficit at Gale crater during southern summer, possibly resulting from
42 a large presence of dust suspended within the crater.

43 **Plain Language Summary**

44   Observations of the permanent CO_2 ice cap at the south pole of Mars in the 2000s
45 suggested that the cap was eroding, possibly releasing a significant amount of CO_2 into
46 the atmosphere. To test this hypothesis, we compare surface pressures recorded by Viking
47 in the 1970s and those recorded by InSight in 2018-2021 to confirm or refute the suspected
48 increase of the atmospheric mass. After establishing our comparison method, we correct
49 for the influence of the sensor temperature on the InSight pressure data, which was dis-
50 covered during our investigation. Comparison of the pressure data, as well as images of
51 the seasonal caps taken by orbiters, do not reveal any change in the atmospheric mass
52 or the dynamics of the seasonal ice caps that develop during the martian year. These
53 conclusions are reinforced by re-exploiting the pressure data recorded by the Curiosity
54 rover. Only small interannual changes are observed, potentially related to the effect of
55 the dust storms that happened on Mars between 2016 and 2018. Finally, we report a pos-
56 sible pressure deficit at MSL's location during southern hemisphere summer, potentially
57 explained by the unusual presence of dust in the crater air.

58 **1 Introduction**

59   The retreat of the Southern Seasonal Polar Cap (SSPC) during local summer leaves
60 a residual perennial deposit mainly composed of CO_2 ice (Kieffer et al., 1972). This de-
61 posit, known as the South Polar Residual Cap (SPRC), is one of the CO_2 reservoirs that
62 can significantly affect the atmospheric mass through sublimation or deposition (Leighton
63 & Murray, 1966). The stability of this reservoir over time is a long-standing debate in
64 Martian climate science. While Blackburn et al. (2010) predicted the disappearance of
65 the SPRC within a few years, Piqueux and Christensen (2008) reported limited changes
66 in the extent and ice-covered area of the SPRC since the Mariner 9 mission in 1972 and
67 telescopic observations in the twentieth century. However, Piqueux and Christensen (2008)
68 were unable to retrieve a mass balance of the cap. Other monitoring of the SPRC sur-
69 face since the Mariner 9 and Viking era led to mass balance estimates suggesting either
70 an erosion of the SPRC (Malin et al., 2001; Thomas et al., 2009; Blackburn et al., 2010;
71 Thomas et al., 2013, 2016) or a possible ice accretion (Thomas et al., 2016). This pre-
72 sumed erosion or accretion of the SPRC open the possibility of secular pressure changes
73 on Mars: if the SPRC loses CO_2 ice year after year, the sublimated CO_2 ice goes into

74   the atmosphere, increasing its global mass and thus also the global mean surface pres-
75   sure on Mars (Malin et al., 2001; Kahre & Haberle, 2010; Haberle & Kahre, 2010; Thomas
76   et al., 2016). Conversely, the deposition of CO_2 ice on the cap would decrease the at-
77   mospheric mass, and thus the atmospheric pressure. Observations from Malin et al. (2001)
78   suggested that the CO_2 ice thickness decreases by nearly 0.4 m per Mars Year (MY),
79   which means an increase of surface pressure of almost +13 Pa per Martian Decade (MD).
80   Blackburn et al. (2010) also estimated a possible increase of surface pressure between
81   +0.5 and +13 Pa/MD. A recent study by Thomas et al. (2016) qualified the two pre-
82   vious estimations by reporting a much smaller variation of SPRC mass balance, with a
83   possible variation of surface pressure between -2.3 Pa/MD and +1.6 Pa/MD.

84   In addition to this possible secular change in atmospheric mass, we can investigate
85   the possibility of an unknown mechanism that would change the dynamics of formation
86   and sublimation of the CO_2 seasonal caps. Thermal infrared observations (Piqueux et
87   al., 2015) or cap albedo monitoring (Calvin et al., 2015, 2017) have already reported in-
88   terannual variability in the formation and recessions of the seasonal caps. However, these
89   studies are limited to a few years of observations, thus preventing a generalization of a
90   possible secular change in the dynamics of seasonal ice caps.

91   A direct way to assess long-term pressure changes on Mars consists of comparing
92   surface pressure measurements separated by several martian decades. By this method,
93   we can check if the atmospheric mass has changed, and study possible variability in the
94   dynamic of the seasonal ice caps. Such a comparison must be done carefully, however,
95   because of the influence of orography and meteorological variability on the annual sur-
96   face pressure cycle (Hourdin et al., 1993, 1995). The comparison of pressure measure-
97   ments made by Viking between 1976 and 1982 and those by Phoenix in 1997, after be-
98   ing corrected for both topography differences and atmospheric dynamics simulated by
99   a Global Circulation Model (GCM), showed a possible 10 Pa rise of surface pressure (Haberle
100   & Kahre, 2010) which corresponds to 5 Pa/MD. However, the combined uncertainties
101   in both the measurements and the interpolation methodology were not sufficiently ac-
102   curate to draw any conclusions about a secular pressure change. More recently, the com-
103   parison between Mars Science Laboratory pressure measurements, which have been recorded
104   since 2012, and Viking measurements did not show significant changes in surface pres-
105   sure (Haberle et al., 2014). However, these conclusions are limited by the sensitivity to
106   the hydrostatic adjustment of surface pressure as the rover is climbing Mount Sharp in
107   Gale Crater (Haberle et al., 2014; Richardson & Newman, 2018), and the sensitivity of
108   the atmospheric dynamics at Gale Crater that have to be resolved by a mesoscale model
109   (Pla-Garcia et al., 2016; Rafkin et al., 2016). Hence, the analysis of the first available
110   surface pressure data neither confirmed nor denied any long-term pressure changes.

111   In 2018, the InSight mission deployed a geophysical and meteorological observa-
112   tory, including a pressure sensor, at the surface of Mars (Banfield et al., 2019; Banerdt
113   et al., 2020). The instruments are deployed on a static lander at Elysium Planitia, a rel-
114   atively flat area located at 4.5° N, 135.6° E (Golombek et al., 2020), thus reducing the
115   sensitivity of surface pressure measurements to both hydrostatic adjustment and atmo-
116   spheric dynamics. Pre-flight calibration and tests suggested that the performances of the
117   sensor were good enough to detect changes in the atmospheric mass and CO_2 cycle (Spiga
118   et al., 2018). We thus propose in this paper to compare the InSight pressure data with
119   the Viking pressure data to assess the possibility of long-term pressure changes over two
120   Mars decades.

121   We present in section 2 the methodology of the pressure interpolation that will lead
122   our comparison between Viking and InSight data. A closer look at the InSight data re-
123   veals a calibration problem due to a sensor temperature sensitivity. We propose an em-
124   pirical recalibration and test the reliability of this correction in section 3. The compar-
125   ison between the InSight corrected pressure data and Viking surface pressure measure-
126   ments is then presented in section 4 to check for a possible secular increase or decrease

127 of atmospheric mass. Long-term variations in the dynamics of the seasonal ice caps be-
128 tween the 1970s and 2018 are also investigated using pressure data and satellite images
129 from the Viking and InSight eras, respectively. We then extend the scope of this study
130 by also exploiting the Phoenix and MSL measurements to detect any evolution of the
131 atmospheric mass in section 5. We also look at the possible influence of interannual vari-
132 ability of the seasonal cap due to the dust cycle. The main conclusions from our inves-
133 tigation are presented in section 6.

2 Methodology of Pressure Interpolation

135 The interpolation of the Viking pressure to the InSight landing site requires tak-
136 ing into account planetary-scale atmospheric dynamics that affect the surface pressure
137 (Hourdin et al., 1993, 1995). Even local interpolation between two close points must in-
138 clude the influence of local weather phenomena, like slope winds. Hence, interpolating
139 pressure cannot be limited to integrating the hydrostatic equation to correct for altitude
140 differences. To take into account the impact of atmospheric dynamics at all scales, we
141 propose two high-accuracy interpolation methods: one on a local scale (typically within
142 a crater, a slope, etc.), and one on a regional-to-global scale.

2.1 Local pressure interpolation

144 We consider here a local situation in which two points are close enough so that large-
145 scale dynamic pressure gradients related to the global atmospheric circulation and re-
146 gional flows can be neglected. Let us consider two points A and B located at different
147 altitudes (Figure 1a). Since these two points are close, the main factor that impacts the
148 difference in the absolute pressure is altitude, thus we could assume hydrostatic equi-
149 librium and recast pressure (P_B) at point B to the altitude at point A ($P_{B \to A}$) with:

$$P_{B \to A} = P_B e^{-\frac{z_A - z_B}{H}} \tag{1}$$

150 where z corresponds to the altitude of each point, H is the scale height expressed as:

$$H = \frac{RT}{\mu g} \tag{2}$$

151 with $R = 8.3145$ J kg^{-1} mol^{-1} the molar gas constant, T is the mean atmospheric tem-
152 perature between A and B weighted by vertical pressure field (in Kelvin), $\mu = 43.34 \times$
153 10^{-3} kg mol^{-1} the mean molecular weight of Mars atmosphere and $g = 3.72$ m s^{-2} Mars'
154 surface gravity.

155 On terrains with an uneven topography, local circulations, like slope winds, can ap-
156 pear as a consequence of temperature gradients. Hence, the choice of a scale height H,
157 and thus the temperature to take into account in Eq. 2, is important to consider the ma-
158 jor effect of these local circulations (Spiga et al., 2007; Forget et al., 2007): the temper-
159 ature choice in H will indicate which path should be used to integrate the hydrostatic
160 equation (red and green lines in Figure 1a). Such effects are very important for the Mars
161 Science Laboratory mission for instance. As the Curiosity rover moves in Gale Crater,
162 with significant gains of elevation (several hundred meters), local circulations and slope
163 winds (Pla-Garcia et al., 2016; Rafkin et al., 2016; Richardson & Newman, 2018) also
164 contribute to the absolute pressure recorded by the rover. Forget et al. (2007); Spiga et
165 al. (2007) suggested using the temperature at an altitude of 1 km above the surface in
166 Eq. 2 to take into account the effect of slope winds at the GCM scale, while Ordonez-
167 Etxeberria et al. (2019) used the air temperature at an altitude of 2 m when using MSL
168 pressure data. Haberle et al. (2014) also questioned the choice of the scale height H that
169 has to be used when exploiting MSL data. Their study of the sensitivity of pressure data

170 to this scale height shows that, with extreme temperature scenarios, the absolute pres-
171 sure can be influenced by several Pascals. However, they never determine which scale
172 height is the right one to use with these data.

173   Thus, we investigate here the scale height that better matches MSL observations,
174 and quantify the errors made during the interpolation of the surface pressure, using the
175 example of Gale Crater. To do so, simulations of Gale Crater with the LMD mesoscale
176 model (Spiga & Forget, 2009) were performed. The domain for the simulations ranges
177 from 22° S to 30° N and 108° E to 163° E, with a spatial resolution of 0.16° , including
178 thus the InSight landing site, Gale Crater and its circulation.

179   We take the diurnal cycle of surface pressure simulated at several seasons at grid
180 points at the bottom (B) and the rim of Gale Crater (A) ($\Delta z = 1725$m, in the axis of
181 MSL trajectory). We then interpolate the pressure at point B (P_B) to location A using
182 several altitudes for the temperature above the point B to compute H. We then com-
183 pute the relative error between the exact modeled pressure at A (P_A), and the interpo-
184 lated pressure from B to A ($P_{B \to A}$). Results are presented in Figure 1b. They show that
185 choosing the temperature at an altitude between 500 m and 2 km above the surface is
186 better to take into account the effect of local dynamics on the pressure interpolation as
187 it minimizes the relative difference between P_A and $P_{B \to A}$. In the following, we choose
188 to compute the scale height H by using the temperature at an altitude of 1 km. When
189 interpolating actual measurements, this temperature is not available from observations
190 and instead has to be estimated using an atmospheric model. The main uncertainty in
191 this calculation results from the sensitivity of temperatures to the dust opacity, which
192 is not perfectly known. To check the sensitivity of the interpolation to these weather con-
193 ditions and thus to an error in T, we use the GCM runs to quantify the impact of the
194 dust opacity using three dust scenarios as input:

195   • A climatology (*clim*) scenario, derived by averaging the available observations of
196   dust from MY 24, 25, 26, 28, 29, 30, and 31 outside the global dust storm period
197   (Montabone et al., 2015). This scenario represents a nominal dust scenario in the
198   absence of major dust storms.
199   • A *cold* scenario which corresponds to an extremely clear atmosphere. At a given
200   date and location, the dust opacity is set to be the minimum observed over Mars
201   years 24-31, further decreased by 50%.
202   • A *warm* scenario which corresponds to "dusty atmosphere" conditions, outside of
203   global dust storms. The dust opacity at a given location and date is set to the max-
204   imum observed over seven Mars years (MY 24-MY 31), excluding the periods of
205   the MY 25 and MY 28 global dust storms, further increased by 50%.

206 These scenarios are used in the Mars Climate Database (MCD, Millour et al. (2018)),
207 and frame well the different temperature observations made by several spacecrafts at a
208 3-σ level (Millour et al., 2018). Using these scenarios, our simulations show that the tem-
209 perature of the air at an altitude of 1 km can vary by several kelvins. We consider the
210 worst-case scenario, assuming that the *cold* scenario decreases the temperature by 10 K
211 compared to the *clim* scenario; and the *warm* scenario increases the temperature by 10
212 K (simulations report a maximum of $\pm$ 8 K in terms of anomaly, and we add a 2 K mar-
213 gin). The relative errors made in the interpolation by using these temperature deviations
214 instead of nominal temperatures are presented in Figure 1c. This sensitivity study shows
215 that the relative 3-σ accuracy of this interpolation method is almost 1%, and is thus ac-
216 ceptable to exploit MSL pressure data. In summary, we found that an accurate way to
217 interpolate surface pressure from a point B to a point A at a local scale consists of us-
218 ing Eq. 1 with the scale height computed using the temperature at an altitude of 1 km
219 above point B (Eq. 2).

220 **2.2 Large-scale pressure interpolation**

221   At the planetary scale, in addition to the hydrostatic adjustment and local dynamic
222 effects, we must take into account large-scale dynamic pressure gradients in the inter-
223 polation (Hourdin et al., 1993, 1995). Hence, interpolating Viking pressure to InSight
224 cannot be done by using Eq. 1 alone, as it does not consider these gradients.

225   To account for these atmospheric large-scale dynamic components, we use a method
226 based on the LMD GCM (Hourdin et al., 1993; Forget et al., 1999). Practically, the in-
227 terpolation of Viking pressure data to obtain the pressure at any location on Mars con-
228 sists of determining the spatial variation of surface pressure in the GCM, with interpo-
229 lation from the coarse GCM topography grid (5.625° in longitude, 3.75° in latitude) to
230 the high-resolution MOLA grid (32 pixels per degree), plus a correction to perfectly match
231 the seasonal variations at the Viking 1 site.

232   Thus, the interpolation of Viking 1 surface pressure at any location, P_s, is done with
233 (Forget et al., 2007; Spiga et al., 2007):

$$P_s = <P_{\text{Viking}}> \frac{P_{\text{GCM}}}{<P_{\text{GCM,Viking}}>} e^{-\frac{z-z_{\text{GCM}}}{H}} \qquad (3)$$

234   where P_{GCM} is the pressure predicted by the GCM at the site we want to inter-
235 polate to, $<P_{\text{Viking}}>$ corresponds to the pressure records of Viking averaged over 15
236 sols to remove any weather variations (thermal tides and transient waves), $<P_{\text{GCM, Viking}}>$
237 is the surface pressure predicted by the GCM at the location of Viking 1 and also smoothed
238 over 15 sols. $z-z_{\text{GCM}}$ is the difference between the MOLA altitude and the altitude
239 defined with the interpolation of the GCM topography grid at the location we consider,
240 and H corresponds to the scale height computed with Eq. 2. The same procedure as the
241 one used in section 2.1, using the GCM pressure field binned every 2 hours, again shows
242 that we must consider the temperature at an altitude of 1 km above the surface. In this
243 expression (Eq. 3), $<P_{\text{Viking}}>$ is the pressure we want to interpolate, $\frac{P_{\text{GCM}}}{<P_{\text{GCM, Viking}}>}$
244 is the correction of atmospheric dynamics induced by the pressure gradients, and $e^{-\frac{z-z_{\text{GCM}}}{H}}$
245 is a hydrostatic correction, taking into account the effect of local dynamics.
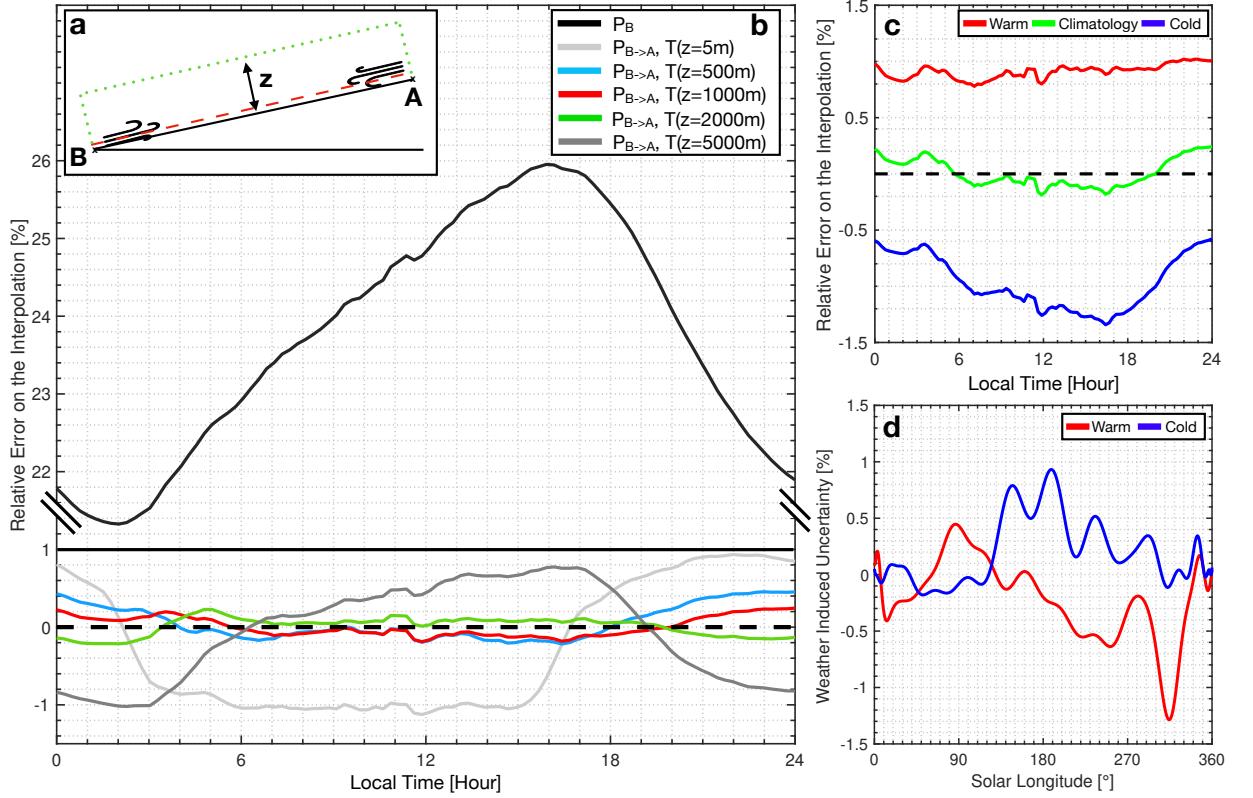
246   We use in this study the Viking 1 surface pressure data rather than Viking 2 data.
247 Viking 1 data are indeed more complete after removing the measurements made during
248 dust storms, less sensitive to baroclinic activity (Ryan & Sharman, 1981; Tillman, 1988;
249 Tillman et al., 1993), and closer to InSight than Viking 2 (Morris & Jones, 1980; Golombek
250 et al., 2020), thus limiting the sensitivity to errors in the correction of the dynamics of
251 the atmosphere.

252   The uncertainty of the interpolation depends on two independent uncertainties: one
253 linked to the Viking 1 pressure measurements and one to the weather-induced uncertainty.
254 On the one hand, pre-flight tests showed that the precision of the Viking pressure sen-
255 sors was better than $\pm 0.2\%$ of the readings, plus a term due to a temperature depen-
256 dency of nearly 0.18% (Seiff & Kirk, 1977; Mitchell, 1977). Consequently, the precision
257 of the pressure measurements was ± 3.4 Pa for Viking 1. Such errors in the precision can
258 be mitigated, however, as we are using a pressure signal averaged over 15 sols. Assum-
259 ing that this precision error on a single measurement can be modeled by white noise with
260 a 3-σ of 3.4 Pa, we can reduce the uncertainty on the diurnal average pressure value by
261 a factor $\sqrt{N}$ where N is the number of measurements used for the diurnal or 15 Sols av-
262 erage. Typically, 200 measurements per sol are used to compute the diurnal average (Barnes,
263 1980). Therefore, by using a 15 Sols averaged surface pressure in Eq. 3, the relative sen-
264 sitivity to the uncertainty of Viking measurements is limited to 0.06 Pa, and is thus com-
265 pletely negligible in the following.

266   On the other hand, Viking measurements are also impacted by systematic errors
267 due to the instrumental drift, the 8-bit telemetry resolution, and the uncertainty on the
268 zero level of the pressure sensor's output voltage. Based on the apparent stability of the
269 sensor because of the great repeatability of the pressure data from one year to another
270 outside dust storm periods (Hess et al., 1980; Tillman et al., 1993), the instrumental drift
271 had been estimated to be only -0.1 ±1 Pa per Earth year and will be neglected in the
272 following. The error due to the 8-bit telemetry resolution (Seiff, 1976; Tillman et al., 1993)
273 yields an uncertainty of 8.8 Pa in the absolute pressure level for one single measurement,
274 even if the sensor has a theoretical resolution of nearly 1 Pa (Hess et al., 1976; Seiff &
275 Kirk, 1977). Assuming that this uncertainty on a single measurement can be modeled
276 by white noise with a 3-σ of 8.8 Pa, and using a 15 sols averaged surface pressure, this
277 uncertainty is reduced to 0.16 Pa and will also be neglected in the following. The last
278 systematic error related to Viking data is due to the uncertainty on the zero level of the
279 pressure sensor's output voltage. This was determined by readings taken just before at-
280 mospheric entry. The resolution uncertainty in these zero readings causes an uncertainty
281 of up to 8.8 Pa in the absolute pressure level (Seiff & Kirk, 1977; Kahanpää et al., 2021).
282 Hess et al. (1980) proposed adding 4.4 Pa to each measurement as it should be the best
283 estimate of the true pressure measurements, reducing the absolute error by half. How-
284 ever, it remains unclear if this adjustment has been implemented in the Planetary Data
285 System (PDS) where data are available. We will thus consider in the rest of the study
286 that the absolute error on Viking 1 pressure measurement is $\Delta P_{\mathrm{Viking}} = 8.8$ Pa at a 3-
287 σ .

288   The second uncertainty in the interpolation is the influence of weather conditions,
289 which impacts T and thus H in Eq. 3 as well as the pressure predicted in the GCM. To
290 study the impact of these conditions on the GCM output, we compute the interpolation
291 of Viking 1 pressure to the InSight landing site by using the three dust scenarios described
292 above, as they bracket well the possible states of the atmosphere (Millour et al., 2018).
293 We then compute the weather-induced uncertainty, defined as the relative difference be-
294 tween the pressure at InSight's location derived with the extreme dust scenarios (*cold*
295 and *warm*) and the *clim* dust scenario (Figure 1d). Figure 1d underlines that this weather-
296 induced uncertainty is generally limited to 1% of the absolute pressure at 3-σ . We set
297 this uncertainty as 1% of the mean annual pressure of 700 Pa at InSight's landing site
298 (Figure 2), i.e., by $\Delta P_{\mathrm{weather}} = 7$ Pa at 3-σ . It should be noted that we use dust sce-
299 narios derived from Mars Climate Sounder (MCS, McCleese et al. (2007)) observations
300 from MY 29 to MY 35 (Montabone et al., 2015, 2020) for our comparisons. The weather-
301 induced uncertainty is therefore much lower as these accurate observational scenarios help
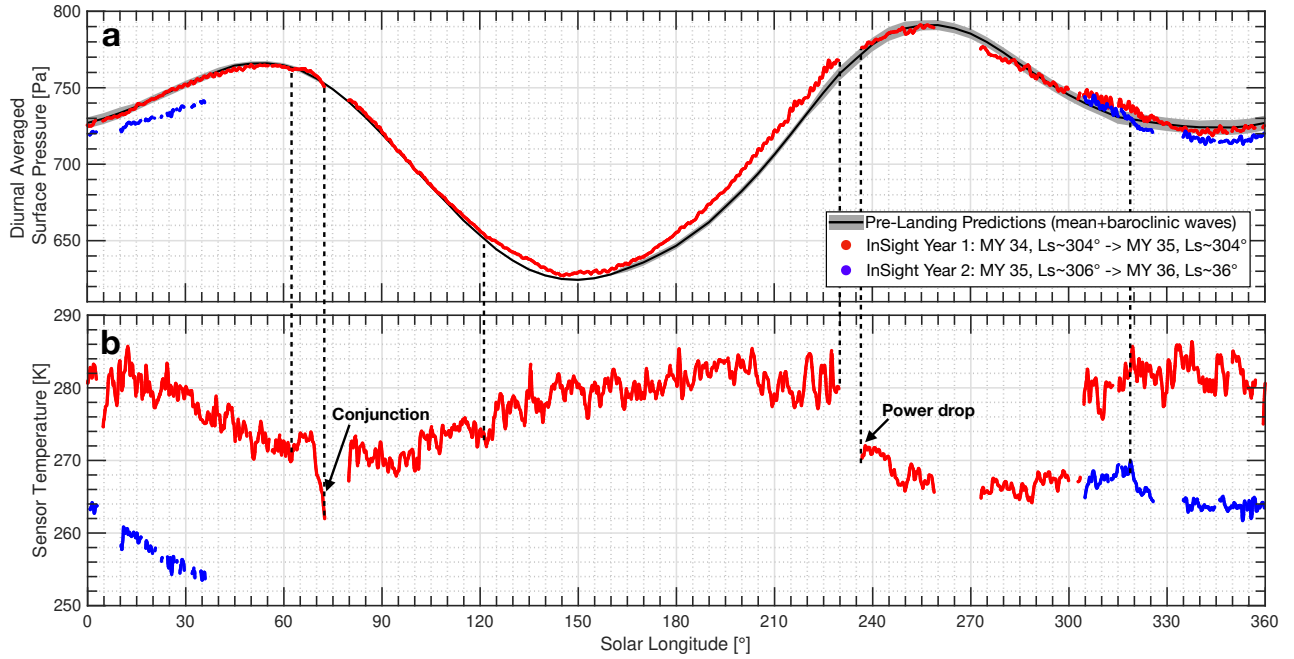302 to compute T, and thus H, in Eq. 3 precisely.

303   Combining the independent uncertainty of Viking measurements $\Delta P_{\mathrm{Viking}}$ and the
304 weather-induced uncertainty $\Delta P_{\mathrm{weather}}$ yields an uncertainty of the interpolation of nearly
305 11 Pa at 3-σ . Such a threshold is at the limit of the lowest predictions of atmospheric
306 mass variations possibly indicated by cap studies (Thomas et al., 2016), but well below
307 the first estimates made at the beginning of the 2000s (Malin et al., 2001; Blackburn et
308 al., 2010).

Figure 1. a) Schematics of the problem of interpolation with slope winds between the bottom of Gale Crater (point B) and the rim of the crater (point A). Colored dots illustrate the different paths that can be taken to integrate the hydrostatic equation. b) Relative error of the interpolated pressure from point B to point A and the exact pressure at A. The black curve is the relative error when point B is not interpolated to point A, while colored curves are for the relative errors when using different altitudes for the temperature. c) Relative error on the local interpolation when using the temperature at 1 km above the surface when considering several kinds of weather scenarios. d) Weather-induced uncertainty of the Viking surface pressure interpolated to InSight landing site computed with extreme dust scenarios when compared to *clim* dust scenario (red and blue curves).

3 Recalibration of InSight Pressure Data

The InSight pressure sensor is located on the lander deck at a height of approximately 1.2 m, with a sampling rate of up to 20 Hz and a noise level lower than 10 mPa, which theoretically represents an unprecedented quality compared to the different pressure sensors that have operated on the surface of Mars (Banfield et al., 2019, 2020; Spiga et al., 2018). These data are calibrated by using output voltage and sensor temperature channels. We use in this study the 20 Hz data and average them with a 50s window to remove any effects of high-frequency pressure events (e.g.,Chatain et al. (2021); Spiga et al. (2021)). We then compute the diurnal average of these signals. To do so, we interpolate the data from previous and following sols to complete the diurnal cycle when there are small gaps (typically of a few hours) in the data. We then interpolate the measurements onto a regular temporal grid containing 100 points per sol. From these interpolated points, we compute the diurnal average. The diurnally averaged surface pressure obtained for the entire dataset (∼1.25 MY) is presented in Figure 2a.

Figure 2. a) Diurnal averaged surface pressure computed from the 20 Hz data acquired during the two years of the mission (red and blue), with pre-landing surface pressure predictions (black curve) and baroclinic waves amplitudes (grey filled area) from Spiga et al. (2018). b) Diurnal averaged temperature of the pressure sensor. Red dots are for the first year of the mission, while blue dots represent the measurements taken during the second year of the mission. Dashed black lines highlight the significant correlations between the sensor temperature and the pressure measurements.

3.1 Sensor temperature sensitivity of the InSight pressure data

A direct comparison between the pressure measurements made one year apart during the first and second Martian years of the InSight mission shows a large difference (Fig. ??). This cannot be explained by the instrumental drift reported in Banfield et al. (2019); Spiga et al. (2018) or by any likely major meteorological event as no significant long-lived global events have been observed. This difference is also not observed by MSL pressure measurements, thus questioning the reliability of the InSight pressure measurements. Furthermore, the divergence between the measurements made two years apart seemed to increase toward the end of the mission, when the power allocated to the pressure sensor was very low because of the accumulation of dust on the solar panels, leading to a decrease of the sensor temperature. A close comparison of the pressure measurements and sensor temperature (Figure 2b) reveals that the pressure measurements are very likely to be affected by some drops or rises in the sensor temperature. An illustration of this correlation is at $L_s \sim 72°$, just before conjunction. Sensors were powered off, after the warm Electronics Box had cooled off, and a nonphysical drop occurred in the pressure measurements. This correlation questions the reliability of the calibration of the absolute pressure data to the sensor temperature. The pre-flight calibration of the pressure sensor with temperature may not be as accurate as expected, possibly because of the existence of temperature gradients within the instrument under real martian conditions. Such an effect had already been identified as responsible for pressure measurement errors on Phoenix (Taylor et al., 2010). It is important to note that most of the scientific results obtained from the pressure data are not impacted by this calibration problem.

345 These works (see for instance Banerdt et al. (2020); Spiga et al. (2021); Chatain et al.
346 (2021)) use relative pressure variations and not absolute measurements, and at high fre-
347 quencies. At these frequencies, i.e., for timescales of the order of a sol, or less, the fluc-
348 tuations of the sensor temperature are negligible. The calibration problem detected is
349 thus nullified when using relative variations of measured pressures, and therefore does
350 not bias the scientific results obtained. We propose in section 3.3 to correct this ther-
351 mal effect using MSL pressure data.

3.2 Mars Science Laboratory pressure data

353 In the absence of major meteorological events, we can expect limited interannual
354 variations between the pressure measured during the first and the second year of the In-
355 Sight mission (see legend of Figure 2 for definitions). de la Torre Juarez et al. (2019) re-
356 ported a strong interannual variability of the pressure data at the end of MY 34 and the
357 beginning of MY 35 compared to other years using MSL pressure data. Such a differ-
358 ence might be linked to the global dust storm of MY 34 that possibly had an impact on
359 the extent of the NSPC.

360 To take into account a possible interannual variability between InSight's first and
361 second years of the mission, we use MSL Rover Environmental Monitoring Station (REMS)
362 pressure data available in the PDS. The calibrated data extracted from the PDS extend
363 from MY 31, at a solar longitude (L_s, the Mars-Sun angle, measured from the North-
364 ern Hemisphere spring equinox where L_s=0°) $L_s \sim$ 150° to MY 36, $L_s \sim$21° . The REMS
365 pressure sensor acquires data during the first five minutes of each Local Mean Solar Time
366 (LMST) with additional hour-long acquisitions that cover a full diurnal about every 6
367 sols (Gómez-Elvira et al., 2014). To take into account the vertical displacement of the
368 rover on pressure measurements, we interpolate the pressure data from the position of
369 the rover determined with the Ancillary Data Record (ADR) files to the MSL landing
370 site using the method described in section 2.1. The air temperatures at an altitude of
371 1 km above the surface are computed with the MCD, using dust scenarios from Montabone
372 et al. (2015, 2020) as inputs for the simulations.

3.3 Recalibration of the pressure measurements

374 We define $E(T(t))$ (in Pa) as the sensitivity of the pressure measurements with re-
375 gards to the sensor temperature T. The corrected measured pressure $P_{InSight,Corrected}$
376 at a time t can be written as:

$$P_{\text{InSight,Corrected}}(t) = P_{\text{InSight,Measured}}(t) + E(T(t)) \tag{4}$$

377 We average the pressure measured by MSL and InSight over 15 sols to eliminate
378 the contribution of any dynamical component like thermal tides and baroclinic activity.
379 These averaged pressure values are denoted $< P >$ in the following. As InSight and
380 MSL are relatively close ($\sim$ 600 km), we assume that the correction of the large-scale
381 atmospheric dynamics between the two sites can be neglected. Our simulations show in-
382 deed that this correction is limited to 1 Pa at 3-σ thus is negligible.

383 During InSight year 1 (Yr_1 : MY 34, $L_s \sim$ 304° to MY 35, $L_s \sim$ 304°) and year
384 2 (Yr_2 : MY 35, $L_s \sim$ 306° to MY 36, $L_s \sim$ 36°) of the mission, we have at first order:

$$\begin{cases} < P_{\text{InSight,Corrected}}(t_{Yr_1}) > = < P_{\text{MSL}}(t_{Yr_1}) > e^{-\frac{\Delta z}{H(t_{Yr_1})}} \\ < P_{\text{InSight,Corrected}}(t_{Yr_2}) > = < P_{\text{MSL}}(t_{Yr_2}) > e^{-\frac{\Delta z}{H(t_{Yr_2})}} \end{cases} \tag{5}$$

385   with Δz the difference of altitude between the InSight and MSL landing site, and H the

386   scale height computed with the air temperature at an altitude of 1 km above the sur-

387   face. GCM computations show that with MY 34, 35 and *clim* dust scenarios, we have

388   to first order $e^{-\frac{\Delta z}{H(t_{Yr_1})}} \sim e^{-\frac{\Delta z}{H(t_{Yr_2})}}$. Thus Eq. 5 leads to:

$$\frac{< P_{\text{InSight,Corrected}}(t_{Yr_1}) >}{< P_{\text{InSight,Corrected}}(t_{Yr_2}) >} = \frac{< P_{\text{MSL}}(t_{Yr_1}) >}{< P_{\text{MSL}}(t_{Yr_2}) >} = \beta \tag{6}$$

389   where β is by definition the interannual variability between the two years of mea-

390   surements. Hence, as we only use a ratio of pressures, the absolute pressure values mea-

391   sured by MSL do not impact the absolute values of InSight pressure measurements af-

392   ter being corrected, and thus do not introduce a bias in our comparison. The problem

393   described by Eq. 6 can be transformed into the following optimization problem:

Find E that minimizes :

$$||< P_{\text{InSight,Corrected}}(t_{Yr_1}) > \ - \ \beta < P_{\text{InSight,Corrected}}(t_{Yr_2}) >|| \tag{7}$$

394   Introducing Eq. 4 into 6 gives:

$$< P_{\text{InSight,Measured}}(t_{Yr_1}) > -\beta < P_{\text{InSight,Measured}}(t_{Yr_2}) >$$
$$= \beta < E(T((t_{Yr_2})) > \ - \ < E(T((t_{Yr_1})) > \tag{8}$$

395   We further assume that E can be written as a polynomial function of the sensor

396   temperature:

$$E(T(t)) = \sum_{k=0}^{n} \alpha_k T(t)^k \tag{9}$$

397   Introducing this into Eq. 8 finally leads to an expression of the function that we

398   want to minimize:

$$< P_{\text{InSight,Measured}}(t_{Yr_1}) > \ - \ \beta < P_{\text{InSight,Measured}}(t_{Yr_2}) >$$
$$= \sum_{k=0}^{n} \alpha_k < \beta T(t_{Yr_2})^k \ - \ T(t_{Yr_1})^k > \tag{10}$$

399   This last equation represents a least-mean-square problem that can be solved nu-

400   merically to determine the coefficients α_k of E for a given degree n. However, the prob-

401   lem must be constrained to have a physical solution. The first term α_0 is indeed poorly

402   constrained as $\beta \sim 1$. A close look at Figure 2 reveals an unexpected increase of the un-

403   corrected pressure at $L_s \sim 63°$, and then a drop, both certainly resulting from a rise of

404   temperature at $T = 270$ K and followed by a decrease of temperature at $T = 275$ K. Such

405   observations are also found at $L_s = 130°$ and $235°$, suggesting a change of behavior of

406   the sensor temperature sensitivity, i.e., a change in the sign $E(T)$ close to $T = 0°$ C. Fur-

407   thermore, the fits used for the calibration of the pressure sensor are good near $T = 0°$ C.
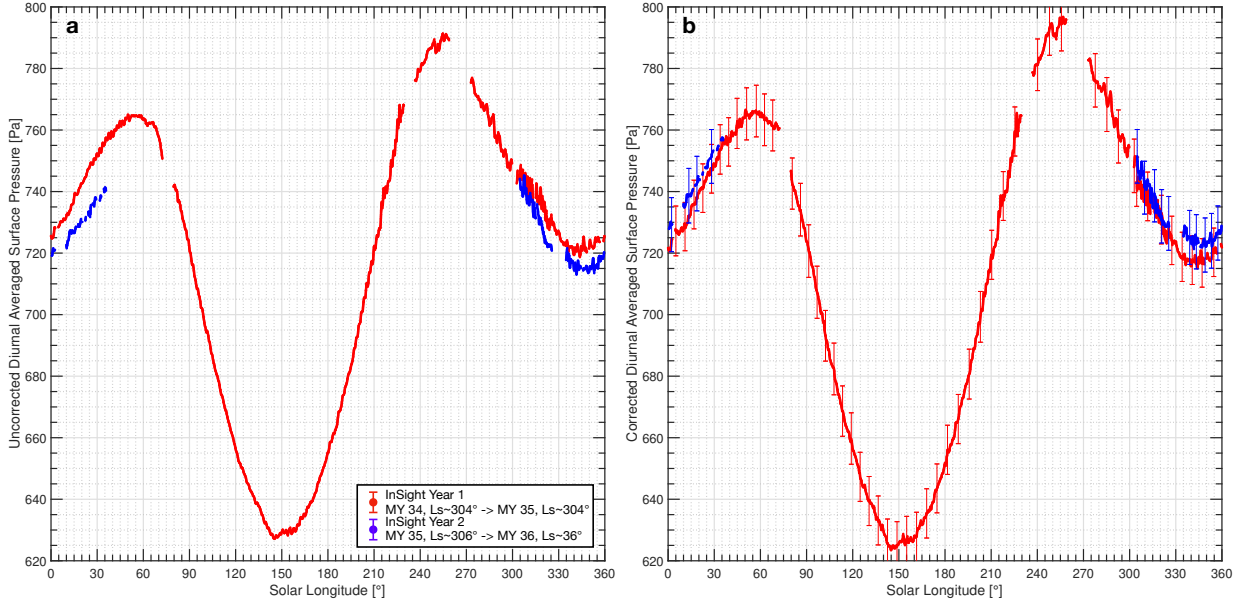
408   Hence we simply assume that:

$$E(T = 0°C) = 0 \ Pa \tag{11}$$

409   The resolution of the problem is made as follow. For each degree n, we compute
410 the coefficients α_k with a least mean square algorithm based on Eq. 10 and 11 to have
411 E. We then compute $|| < P_{\text{InSight,Corrected}}(t_{Y r_1}) > - \beta < P_{\text{InSight,Corrected}}(t_{Y r_2}) >||$
412 using Eq. 4. We iterate on the degree n to find which E is solution of the optimization
413 problem described in Eq. 7.

414   To compute the least-mean square inversion, we use the data acquired at the end
415 of the MY 34, at $L_s > 340°$ to remove the effect of local dust storms, and data at $L_s < 21°$ (the
416 limit of the MSL dataset that we used). We finally find that the correction E can be writ-
417 ten as:

$$E(T) \approx 5.5273 \times 10^{-4}\, T^3 - 0.4284\, T^2 + 109.6849\, T - 9.2602 \times 10^3 \qquad (12)$$

418   Applying this correction to the complete measured pressure data with Eq. 4 leads
419 to the result presented in Figure 3. As expected, this correction strongly modifies the
420 pressure measured by InSight in terms of amplitude and shape. The Northern winter sur-
421 face pressure during InSight Year 1 is lower than during InSight Year 2, but tends to equal-
422 ize during spring. These results are thus consistent with the analysis of contemporary
423 MSL data from de la Torre Juarez et al. (2019).

Figure 3.   a) Diurnal averaged surface pressure computed from the raw pressure data. b) Diurnal averaged surface pressure after applying the thermal correction. Error bars represent the uncertainty on the measurements after the correction at 3-σ . The details of the uncertainty computations are described in the text. Red dots are for the first year or the mission, while blue dots are for the second year.

3.4 Uncertainty of the corrected data

425   The accuracy of InSight pressure measurements is crucial for the determination of
426 possible secular pressure changes and will be useful to the community for future scien-
427 tific work. We thus need to quantify the uncertainty of the InSight corrected pressure
428 proposed in section 3.3. Three kinds of uncertainty can be highlighted here according

429 to Eq. 4. The first one is the uncertainty of the pressure sensor on the measurement, which
430 is $\sigma_{P_{sensor}} = 1.5$ Pa R.M.S (Banfield et al., 2019). The second one is caused by the un-
431 certainty of the correction. This correction deals with the uncertainties at 1-σ of the pres-
432 sure measured by InSight $\sigma_{P_{sensor}}$ and the sensor temperature uncertainty σ_T set here
433 at 1 K. However, the uncertainty of β, and thus the impact of MSL uncertainty on our
434 correction, is negligible. ($\frac{\sigma_\beta}{\beta} \ll 1$, Appendix A). Hence, as we use a ratio of MSL pres-
435 sure measurements to derive the interannual variability β of the InSight pressure data,
436 the absolute MSL pressure accuracy does not impact the accuracy of our correction for
437 the InSight pressure measurements. Finally, an uncertainty is associated with the choice
438 of the temperature nullifying the correction term (Eq. 11); this last one having been made
439 arbitrarily after analysis of the correlations between the measured pressure and the sen-
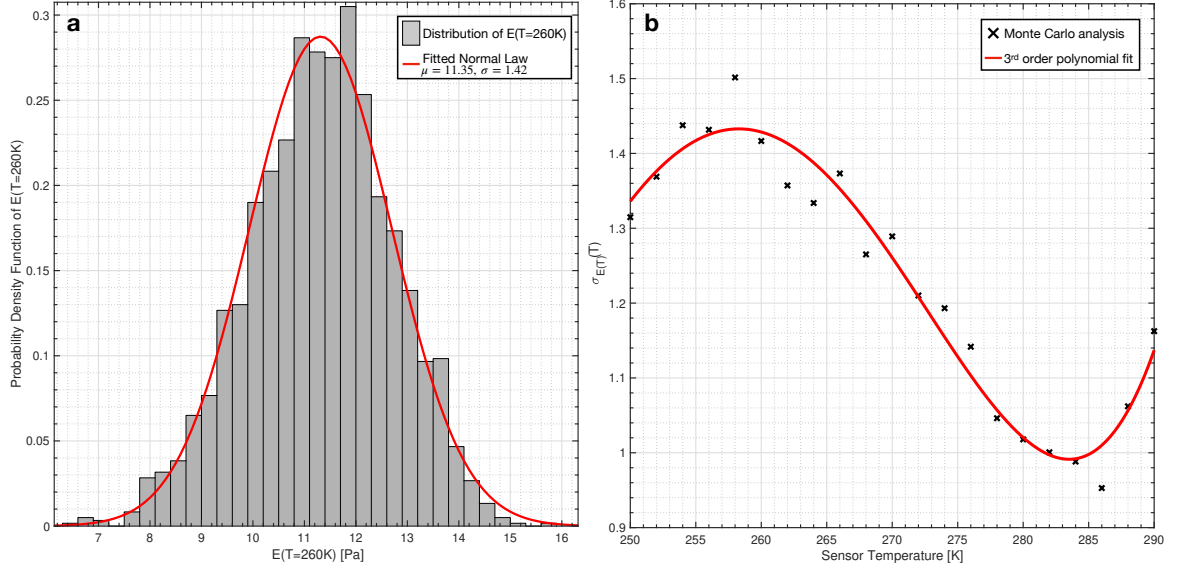440 sor temperature.

441   To derive the uncertainty in E at a sensor temperature T ($\Delta E(T)$), we perform
442 a Monte Carlo error analysis as described in Press et al. (1993) or Forget et al. (2007).
443 We generate an ensemble of 10^4 inputs (P_{InSight},T), affected by the various uncertain-
444 ties described above. All the input parameters are computed using their nominal val-
445 ues plus random values computed from a normal distribution with a standard deviation
446 associated with $\sigma_{P_{sensor}}, \sigma_T$. The condition provided in Eq. 11 is also perturbed using
447 a normal distribution with a standard deviation of σ_T. We then apply our algorithm to
448 retrieve the thermal correction E at a given temperature T with these inputs. We finally
449 compute the standard deviation of the E provided. We find that the distribution of the
450 E retrieved follows a normal distribution as illustrated in Figure 4a. The standard de-
451 viation of the fitted normal distribution gives the uncertainty of $E(T)$ at 1-σ . We ap-
452 ply this Monte Carlo analysis for temperatures ranging from 250 K to 290 K to retrieve
453 $\sigma_{E(T)}$, i.e., the uncertainty at 1-σ level. The results from this computation are presented
454 in Figure 4b. The variations of this curve follow the variations of the gradient of $E(T)$.
455 We then do a least mean square polynomial fit to have an empirical law to simply de-
456 duce $\sigma_{E(T)}(T)$:

$$\sigma_{E(T)}(T) = 5.1453 \times 10^{-5}\, T^3 - 0.0418\, T^2 + 11.2738 \times\, T - 1.0109 \times 10^3 \qquad (13)$$

457   We finally retrieve the 3-σ uncertainty of one pressure measurements by combin-
458 ing these two uncertainties, plus a term due to the dependence between the measurement
459 and the thermal correction, as the raw measurements and temperature are correlated due
460 to the initial calibration procedure:

$$\Delta P_{InSight}(T) = 3 \times \sqrt{(\sigma_{P_{sensor}})^2\, +\, (\sigma_{E(T)}(T))^2\, +\, 2\sigma_{P_{sensor}}\sigma_{E(T)}(T)\rho_{P_{sensor},T}} \qquad (14)$$

461 where $\rho_{P_{sensor},T}$ is the correlation coefficient between the raw pressure measurement P_{sensor}
462 and the sensor temperature (T), assumed to be 1 as the pressure sensor is calibrated us-
463 ing the sensor temperature (Banfield et al., 2019). Uncertainties on the corrected pres-
464 sure range from 7.5 Pa to 8.9 Pa at a 3-σ level. Such values are close to the magnitude
465 of the atmospheric mass variations expected based on Thomas et al. (2016)($\pm$ 9 Pa dif-
466 ference between Viking 1 and InSight surface pressures), but are much smaller than the
467 expected changes that are computed from Blackburn et al. (2010); Malin et al. (2001)($\sim$+25
468 Pa difference between Viking 1 and InSight surface pressure). We therefore consider that
469 the InSight corrected pressure data are accurate enough to detect such secular pressure
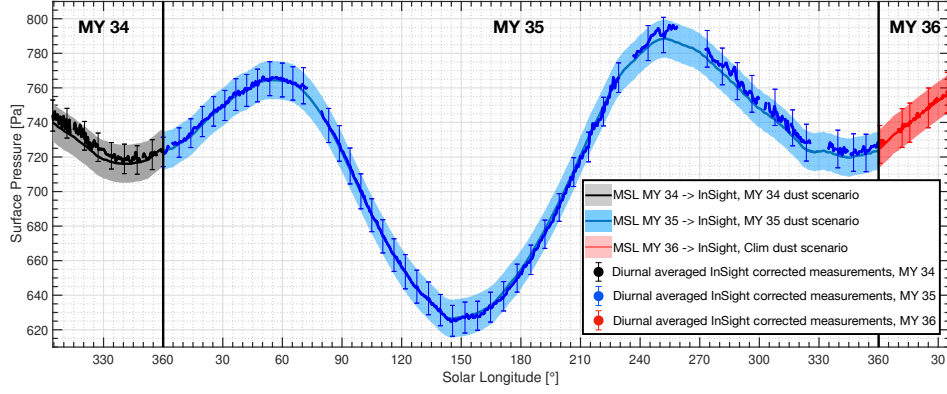470 changes.

Figure 4. a) Monte Carlo analysis to retrieve $\sigma_{E(T=260K)}$. The histogram of the samples is presented in gray and is normalized to obtain a probability density function. The fitted normal law is illustrated in red and has as parameters the mean μ and the standard deviation of the distribution σ. b) Empirical law for $\sigma_{E(T)}(T)$ obtained from Monte Carlo analysis (black cross) and 3rd order polynomial fit of this law (red line)

3.5 Comparison with MSL pressure data and validation

472   To test the reliability of our correction, we propose here to compare the corrected
473   InSight pressure to the MSL pressure measurements interpolated to the InSight land-
474   ing site. This comparison is relevant as the use of the MSL data to correct the InSight
475   data relied on the year-to-year ratio (Eq. 6), and thus does not influence seasonal vari-
476   ation given by InSight pressure data after the correction. To do so, we use the method-
477   ology described in 2.2 by using the ratio $\frac{P_{MSL}}{P_{GCM,MSL}}$ into Eq. 3, with MY 34,35 and *clim*
478   dust scenario for the beginning of MY 36. The comparison between interpolated MSL
479   pressure and InSight measurements is presented in Figure 5. There is an overall good
480   agreement between the InSight corrected measurements and the MSL pressure measure-
481   ments. This consistency strengthens the credibility of our correction.

482   We note a deficit δ of pressure between MSL pressure interpolated at the InSight
483   landing site, and InSight corrected pressure between $L_s \sim 200°$ and $L_s < \sim 360°$ (Fig. 5).
484   Three causes could explain this deficit: 1) a dynamical effect that is not included in our
485   interpolation process 2) a meteorological effect that changes the thermal state of the at-
486   mosphere, and thus the scale height used during the interpolation 3) a problem with our
487   correction.

488   As InSight and MSL are close to each other (~ 600 km), the impact of atmospheric
489   dynamics on the interpolation is limited. As underlined by Figure 5, large-scale atmo-
490   spheric dynamics does not explain the pressure difference. Another possible explanation
491   might be the small-scale/regional topography of Gale crater that is not included by our
492   GCM. The two closest points are at a longitude of 135° E and 140.6° E, with an altitude
493   of -2069 and -1879 m respectively. The interpolation using the four closest points of the
494   GCM to the MSL landing site gives an altitude of -1544m, far from the actual landing
495   site altitude of -4501 m. Furthermore, complex crater circulations (Pla-Garcia et al., 2016;
496   Rafkin et al., 2016) might impact the pressure measured by MSL. To investigate this deficit,

Figure 5. Comparison between the surface pressure measured by InSight and that measured by MSL but interpolated to the InSight landing site, for MY 34, 35, and 36. The filled box around the plain line depicts the 3-σ uncertainty of the interpolation due to weather-induced uncertainty and MSL absolute errors, following the methodology presented in section 2.2. Pressure interpolated is averaged over a period of 15 sols to remove atmospheric tides and baroclinic activity. InSight measurements are diurnally averaged thus still indicate baroclinic activity with periods of several sols. The error bars correspond to the 3-σ on InSight corrected pressure measurements as described in section 3.4.

497   we used the mesoscale LMD model simulations described in section 2.1. We ran the model
498   for 24 hours after initial spin-up time of 24 hours, at $L_s = 270°$. The mesoscale model,
499   representing a more accurate topography and capturing local circulations, helps to re-
500   duce the pressure deficit between MSL interpolated to InSight and InSight measurements
501   but still not fully explain the difference observed. Hence, the deficit δ does not seem to
502   be due entirely to a dynamic effect.

We then studied this deficit δ by investigating the possible influence of the scale height H, using the interpolation described in 2.1. Results are presented in Figure 6a. We observe again the pressure deficit between InSight and MSL after $L_s = 180°$. To study the influence of the scale height, we compute the temperature T_* such that: $\frac{<P_{\text{MSL}\rightarrow\text{InSight}}>}{<P_{\text{InSight}}>} \approx 1$. Using Eq. 1 and 2, T_* writes:

$$T_* = -\frac{\Delta z}{\frac{R}{\mu g} \ln \frac{P_{\text{MSL,measured}}}{P_{\text{InSight,measured}}}} \tag{15}$$

503   where Δz correspond to the difference of altitude between the InSight landing site and
504   MSL altitude (in meters), and $P_{MSL,measured}$ is the raw MSL REMS pressure measure-
505   ments. To detect any anomaly in the temperature, we compare this temperature T_* to
506   the temperature at an altitude of 1 km above the surface predicted by the GCM (Fig-
507   ure 6b). This comparison underlines warming by 10-15 Kelvin of the temperature at this
508   altitude, at $200° < L_s < 360°$.

509   This difference between T_* and the temperature given by the GCM could be ex-
510   plained by an unexpected accumulation of aerosols within Gale Crater, such as dust, com-
511   pared to what is assumed in the GCM. The presence of aerosols would indeed warm up
512   the air as they absorb solar radiation. Moreover, GCM simulations using our *warm* sce-
513   nario indicate a warming of nearly 5-8 K of this atmospheric layer, which is the order
514   of magnitude of the anomaly observed here. Hence, by studying the evolution of the tem-
515   perature anomaly presented in Figure 6b, we could assume that at $L_s > 180°$, there are
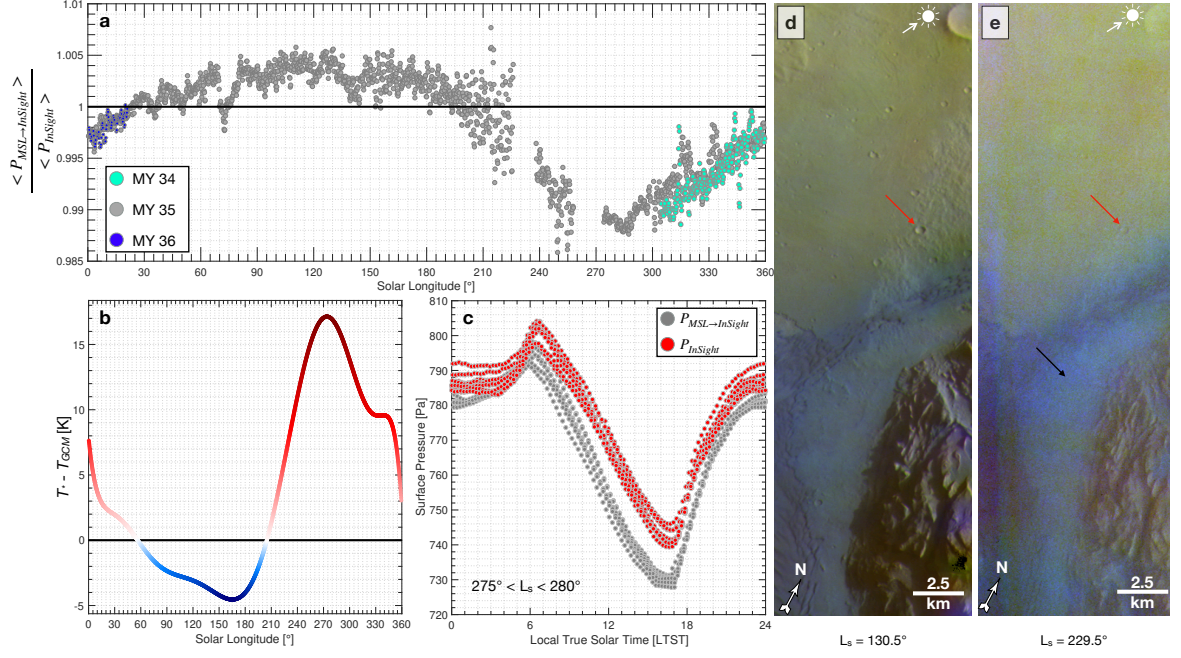516   local effects that increase the quantity of dust or other aerosols within the crater, induc-

517 ing a warming of the air temperature. By comparing the measured and interpolated pres-
518 sures at different local times around $L_s = 275°$(Figure 6c), we find that this pressure anomaly
519 occurs during the day. We can assume that the air within the crater is heated during
520 the day due to the presence of this dust in suspension. This hypothesis is consistent with
521 the REMS temperature observations at the surface and at 2 m from the ground at this
522 time of year, which are respectively lower and higher than predicted by mesoscale mod-
523 els (Pla-Garcia et al., 2016).

524   Several observations reinforce the credibility of this scenario. Measurements of the
525 line-of-sight across-crater extinction with MSL cameras report an increase of dust load-
526 ing at lower elevations during the dusty season, i.e., $180° < L_s < 360°$. The analysis of
527 UV sensors data onboard MSL also confirms this observation, with net dust lifting from
528 the crater floor during the dusty season, and net deposition during the rest of the year
529 (Vicente-Retortillo et al., 2018). Such observations confirmed models of dust diffusion
530 rate within Gale crater (Moore et al., 2019) that report net dust lifting from $L_s \approx 220$-
531 240°, and net dust deposition in the crater before this date, explaining the variation of
532 the thermal inertia of the ground (Rangarajan & Ghosh, 2020). This behavior of set-
533 tling and suspension of dust within Gale might be explained by the dynamics of the plan-
534 etary boundary layer within the crater. Fonseca et al. (2018) points out that at $L_s > 180°$,
535 the planetary boundary layer (PBL) height is higher than the crater rim for a few hours
536 during the afternoon, inducing a mixing between the air outside and inside the crater.
537 In addition, dust migh be injected within the crater because of dust devils and wind-driven
538 dust lifting. As reported by (Steakley & Murphy, 2016; Kahanpää et al., 2016; Ordonez-
539 Etxeberria et al., 2018; Newman et al., 2019), there are very strong seasonal variations
540 in dust devil activity, with a peak of that dust devil lifting around southern spring and
541 summer, i.e., when we observed the pressure deficit δ. Most of the dust devil occurs dur-
542 ing the day, with a peak of activity around noon, close to the period of the sol when the
543 pressure difference between MSL and InSight is the most important (Fig. 6c).

544   We also obtain indications of the presence of aerosols near the surface using the
545 THEMIS visible camera (Christensen et al., 2004). Figures 6d and e compare two im-
546 ages of Gale Crater, at the same local hour, in quasi-similar illumination conditions, but
547 at two different L_s(130° and 229° respectively). Figure 6e clearly shows the presence
548 of aerosols (black arrow) confined within the crater, as the portion of Mount Sharp re-
549 mains easily detectable and less obstructed. Another indication of the presence of a sig-
550 nificant quantity of aerosols in the air is the difficulty of detecting the ground and the
551 craters at the bottom of Gale crater on the image e compared to d (see red arrows), in
552 quasi-similar illumination conditions. Water fog is a suspected candidate to explain this
553 phenomenon, as the image is taken during the early morning, but it seems highly un-
554 realistic as the relative humidity at this time of the year is at its lowest level (Martínez
555 et al., 2016; Martínez et al., 2017). Furthermore, images taken at nearly 17 hr Local True
556 Solar Time (LTST) also report such features (see for instance THEMIS image *V59356002*
557 that were taken at a quite similar location at $L_s = 335°$, at 17.37 hr). However, opac-
558 ity derived from MSL cameras does not show a significant increase of dust loading at this
559 time, compared to what is predicted by the *clim* scenario (see Figure 9 of Ordonez-Etxeberria
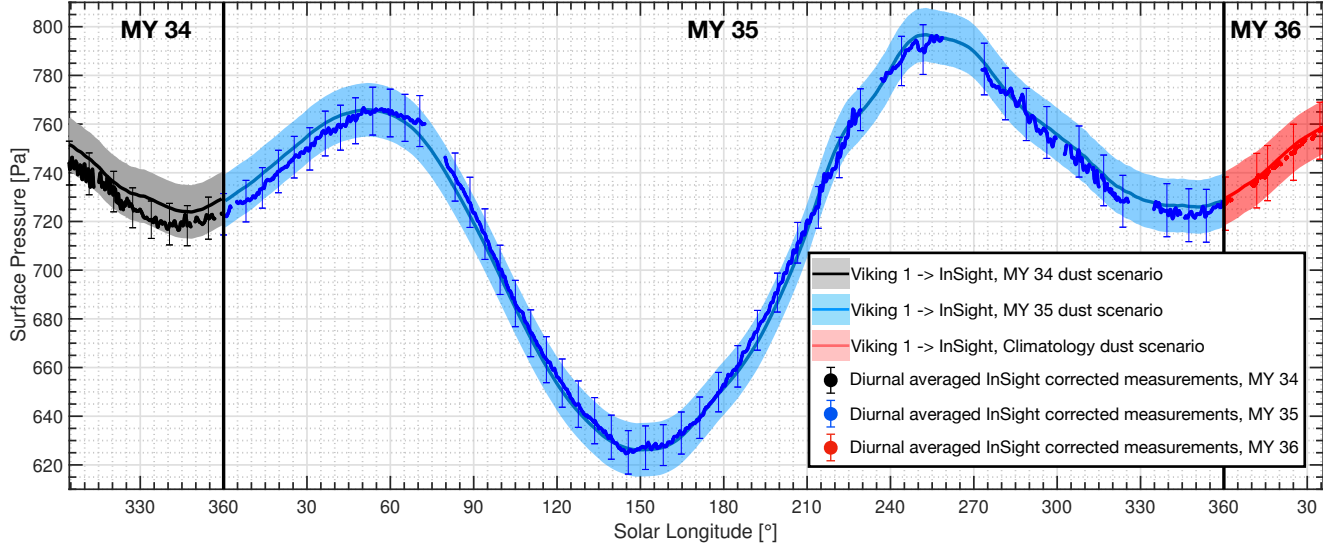560 et al. (2019)).

561   Hence, even if we have several indications making credible our scenario of dust in
562 suspension that explains the temperature anomaly within Gale Crater, further investi-
563 gations are required to confirm this assumption, including an analysis of UV fluxes for
564 instance. This hypothesis, however, has the potential to explain the observed deficit, and
565 thus does not cast major doubt on our correction to the InSight pressure data. A ma-
566 jor mistake in our correction seems unlikely because of the very good agreement between
567 the pressure measurements of MSL and InSight during the rest of the year.

Figure 6. a) Evolution of the ratio of MSL REMS pressure measurements interpolated to the InSight landing site, and InSight pressure measurements. Dots correspond to the ratio using the interpolation method described in section 2.1, i.e., neglecting atmospheric dynamic effects, during MY 34 (green), MY 35 (grey), and MY 36 (blue). b) Anomaly between the temperature of the GCM at an altitude of 1 km above the surface, and the temperature T_* that gives a ratio of 1, as a function of L_s (colored curve) for MY 35. c) Comparison between InSight surface pressure over a complete sol and MSL pressure interpolated at InSight landing site between $L_s =$ 275° and 280°, during MY 35. d) Extract of THEMIS image *V63417011* of Gale Crater (center of the original image: 4.9°S;137.0°E) taken at $L_s =$ 130°, LTST = 7.2hr, with a solar incident angle of 74.5°. e) Extract of THEMIS image *V65575024* at the same location, taken at $L_s =$ 229°, LTST = 7.2hr, with a solar incident angle of 71.3°. The black arrow on e) points to the suspected aerosols, whereas the red arrows on d) and e) point to the same crater for a comparison of the perceptibility of the ground. White arrows point to the position of the Sun in the sky.

4 Results: Comparison with Viking Lander 1 Pressure Data

Figure 7. Comparison between the surface pressure by Viking 1 interpolated at the InSight landing site for MY 34, 35, and 36. The filled box around the plain line depicts the 3-σ uncertainty of the interpolation detailed in section 2.2. Pressure interpolated is averaged on a period of 15°to remove atmospheric tides and baroclinic activity. InSight measurements are diurnal averaged and still keep baroclinic activity. The error bars correspond to the 3-σ on InSight corrected pressure measurements as described in section 3.4.

The comparison between the Viking 1 surface pressure measurements interpolated at the InSight landing site and the InSight temperature-corrected measurements for MY 34, 35, and 36 is presented in Figure 7. During MY 34 and the beginning of MY 35 (L_s<55°), InSight pressure measurements are lower compared to Viking 1 pressure by 5-10 Pa. de la Torre Juarez et al. (2019) also reported a pressure deficit at these times when studying the repeatability of MSL pressure data. Using MCS thermal data, they relate this to a possible increase of the NSPC expansion during MY 34 compared to MY 33. Such an expansion would consequently decrease the atmospheric mass at this time, reduce the surface pressure, and thereby explain the deficit observed. This deficit is not observed during Northern winter of MY 35 with MSL and InSight pressure data, and thus cannot be linked to a secular change.

After the sublimation of the NSPC during MY 35, the InSight pressure measurements match Viking pressures very well within the uncertainties associated with the interpolation method. The weather-induced uncertainty might explain the small deficit of pressure observed at L_s>250°because Viking 1 pressure was more affected by baroclinic activity as the lander is at a higher latitude than InSight. There is also smaller confidence in the Viking 1 pressure average during this period, as a lot of the measurements available at this time of the year were affected by the first global dust storm recorded by Viking (Ryan & Sharman, 1981), and thus removed from the dataset.
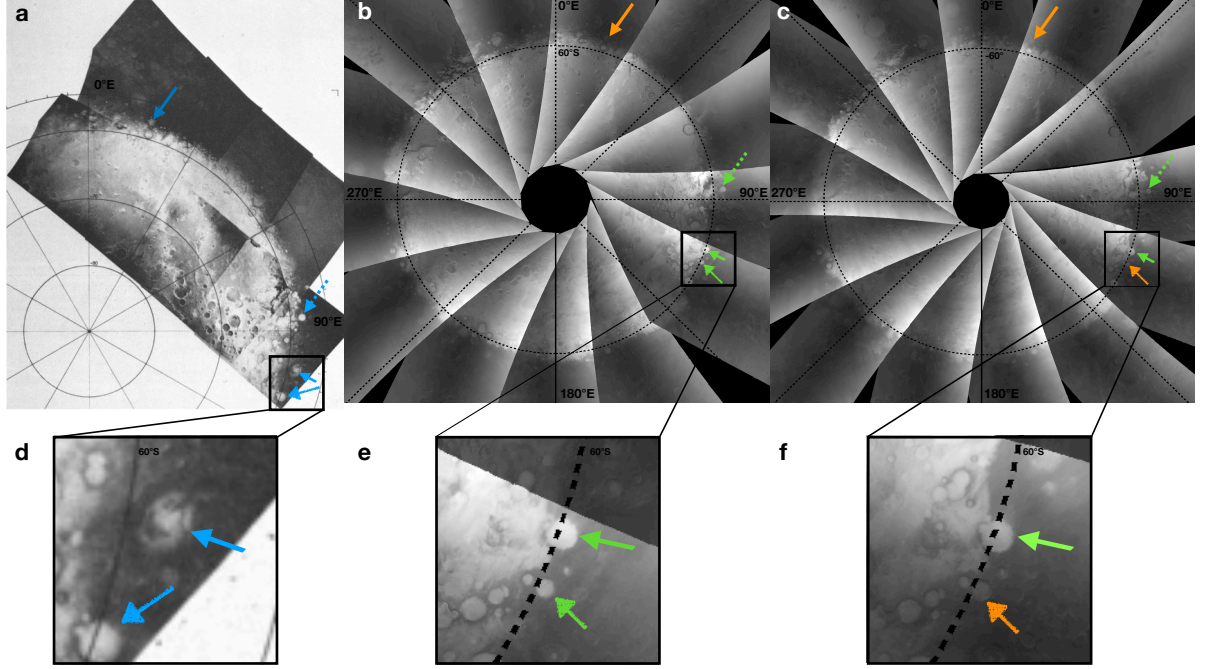
However, the overall strong agreement between Viking 1 interpolated surface pressure and InSight thermally corrected measurements strongly supports the assumption that the atmospheric mass has not changed since the Viking era, nearly forty earth years

591 before the InSight era. Our results suggest that SPRC mass balances from Malin et al.
592 (2001); Blackburn et al. (2010) might have been overestimated, but support low estimated
593 values of atmospheric mass gain/loss due to the evolution of the SPRC (Thomas et al.,
594 2016). Such results thus reinforce the assumption that the SPRC does not suffer from
595 major changes over decades, as indicated by both imagery comparisons since the Mariner
596 era and recent imagery dataset (Piqueux & Christensen, 2008; Thomas et al., 2016). In
597 fact, the SPRC might be varying with periods of erosion due to large summer dust events,
598 followed by a period of deposition in the next winter (Bonev et al., 2008; Becerra et al.,
599 2015; Byrne et al., 2015; James et al., 1992, 2010; Thomas et al., 2016). Further discus-
600 sion on the role of dust events in the condensation and sublimation of CO_2 ice is shown
601 in section 5.2. The possible influence of CO_2 reservoirs under the SPRC on the dura-
602 bility of this cap has also been explored recently (Buhler et al., 2020).

603 The strong agreement of the surface pressure comparison during the formation and
604 sublimation of seasonal caps (excluding the Northern winter of MY 34) also suggests a
605 low variability of the martian seasonal CO_2 cap dynamic. This result is consistent with
606 those of Piqueux et al. (2015) using infrared spectroscopy, or those obtained using albedo
607 monitoring (James, 1979, 1982; James & Lumme, 1982; Calvin et al., 2015, 2017). These
608 studies cannot detect changes over decadal timescales, however, as these comparisons are
609 limited to observations separated by a few martian years, or use telescopic observations
610 of the twentieth century that are potentially less accurate (James et al., 1987; Piqueux
611 & Christensen, 2008). We propose here to track possible secular change on the season-
612 ality of these caps by making a comparison of the caps' albedo. To do so, we exploit im-
613 ages of the SSPC taken by Viking Orbiter 2 during MY 12 (James et al., 1979) and MARCI
614 images (Malin et al., 2001) taken during MY 35 (images from MY 34 are not used be-
615 cause of the global dust storm that occurred during this year, hindering the visual de-
616 tection of the caps). Piqueux et al. (2015) noted interannual variability in the caps' dy-
617 namics due to global dust storms. We thus add MY 33 to the comparison as a control
618 year in case the global dust storm at the end of MY 34 influenced the cap dynamics dur-
619 ing MY 35. Furthermore, even if the cap boundary is composed of water ice after the
620 sublimation of the seasonal CO_2 ice (see the spectroscopic study in Langevin et al. (2007)),
621 we assume that albedo comparison between the Viking decade and late 2010s/early 2020s
622 also reflects possible changes in the CO_2 cycle.

623 Details on the composition of MARCI polar mosaic are given in Calvin et al. (2015,
624 2017). We select $L_s = 192.6°$ for the comparison as Viking mosaic is available at this time
625 (Figure 5 of James et al. (1979)). Similar analysis and conclusions can be drawn using
626 other L_s. The comparisons are presented in Figure 8. On Viking images, we flag with
627 blue arrows craters or easily distinguishable topographies that are covered by ice at the
628 boundary of the cap. We then look at MARCI images to see if the element is still cov-
629 ered by ice at the same time of the year. In this case, the element is flagged by a green
630 arrow, whereas in the case of a divergence with Viking observations, the element is flagged
631 by a red arrow. In case of doubt about the presence of ice, we flag the crater with an
632 orange arrow. The comparisons underline that no major changes have happened in the
633 dynamic of the seasonal caps, thus confirming what has been observed by comparing Viking
634 1 and InSight pressure data. Little variability can be noted as revealed by the orange
635 arrows. It can be explained by some observational biases. First, MARCI mosaics are built
636 with images taken during all the day, and at different LTST. Hence, some ice might have
637 sublimated during the day and would not be present on the mosaic. Second, the discrep-
638 ancies on Fig. 8f are actually a consequence of the timing of the mosaic, as the images
639 are not taken exactly at the same L_s and illumination conditions. At least, it is very un-
640 likely that these discrepancies observed are due to a faster retreat of the seasonal cap
641 as a consequence of the MY 34 global dust storm. Our GCM simulations show indeed
642 that this retreat should occur at the same speed between MY 33 and 35.

643   Thus, the comparison between Viking 1 and InSight pressure data, as well as the
644 comparison of images taken by the Viking 2 orbiter and the MARCI camera suggest the
645 absence of secular pressure changes or modifications in the dynamics of the seasonal ice
646 caps.

Figure 8. Comparison of the SSPC images taken by (a) Viking orbiter during MY 12, $L_s = 192.6°$ (extracted from James et al. (1979)); (b) MARCI during MY 33, $L_s = 192.3°$; and (c) MARCI during MY 35, $L_s = 192.9°$. Blue arrows flag characteristic surface features for the comparison like craters. Orange arrows indicate a possible difference between the Viking images and MARCI images while green arrows indicate a good match between the images. d) to f) are zoom on the lowest flagged craters of a), b), c). The 60°S circle of latitude on image d) extracted from James et al. (1979) is misplaced, but arrows point to the same elements.

5 Discussion

5.1 Evolution of the atmospheric mass since MY 29

649   The non-detection of atmospheric mass changes between the 1970s and present dis-
650 agrees with the conclusions obtained from the comparison between Viking and Phoenix
651 surface pressure made in (Haberle & Kahre, 2010). The preliminary comparison between
652 MSL and Viking 2 pressure data, which are nearly at the same altitude above the sur-
653 face, did not show any significant increase of the atmospheric mass, but rather possibly
654 a small decrease. We propose to extend this analysis by also comparing Phoenix and MSL
655 data with Viking 1 pressures, using our methodology

656   presented in section 5.1 for the comparison between Viking 1 and InSight pressure.
657 Phoenix data used here are extracted from Taylor et al. (2010), as they are thus corrected
658 from the temperature gradient within the sensor that disturbed the measurements (Taylor
659 et al., 2010). The results are presented in Figure 9.

Figure 9. a) Comparison of the surface pressure measured by Phoenix (green dots), MSL (blue dots), and InSight (red dots), to Viking 1 measurements (interpolated at each landing sites), from MY 29 to MY 36. Yellow boxes correspond to periods of local dust storms at landing sites (Holstein-Rathlou et al., 2010; Ordonez-Etxeberria et al., 2019), while the orange box corresponds to the period of MY 34 global dust storm (Viúdez-Moreiras et al., 2019). b) to d) Evolution of the relative difference between Viking 1 interpolated and MSL (blue) and InSight (red), as a function of Martian Year at $L_s = 20°$(b), $L_s = 170°$(c), $L_s = 310°$(d). The error bars indicate the sensitivity of the comparison with regards to the interpolation uncertainty at 3-σ , as described in 2.2.

660   Figure 9a underlines an excess of pressure when comparing Phoenix measurements
661 to Viking 1 interpolated to Phoenix landing site. Such result is consistent with the anal-
662 ysis from Haberle and Kahre (2010). However, the location of Phoenix must be consid-
663 ered and might qualify their conclusions. Phoenix landed at a high latitude (68.22°N)
664 compared to the other measurements used in this study that were made at mid/equatorial
665 latitudes. This difference could lead to errors in our interpolation due to the large lat-
666 itudinal pressure gradients. The error bars in Figure 9a underlines that the difference
667 lies within the 3-σ uncertainty of our interpolation method. Hence, it is difficult to con-
668 clude on a possible increase of atmospheric mass in MY 29 using Phoenix measurements
669 only. These observations might actually illustrate a real rise of the atmospheric mass due
670 to a significant SPRC erosion during the MY 28 global dust storm (Montabone et al.,
671 2015). Bonev et al. (2008); Becerra et al. (2015); Byrne et al. (2015); Thomas et al. (2016)
672 report that southern spring/summer dust storms, like the one in MY 28, might enhance
673 the SPRC sublimation, which would consequently increase the atmospheric mass. Fur-
674 ther observations like an analysis of the SPRC extent between MY 27, 28, 29 should help
675 to find the explanation of this increase of the surface pressure at the Phoenix landing
676 site.

677　　　　The comparisons of MSL and InSight data with Viking 1 pressure measurements
678　both show the same results, i.e., an excess of pressure for $90° < L_s < 180°$, and a deficit
679　elsewhere. Such divergences are small (less than 1% generally) and both comparisons
680　are consistent, i.e., MSL and InSight present a deficit or excess of pressure at the same
681　time of the year, but MSL data have sometimes larger relative differences. We study with
682　Figures 9b to d the evolution of these divergences to Viking interpolated pressure, at three
683　times of the year: $L_s = 20°, 170°, 310°$. No clear trend can be established when compar-
684　ing MSL or InSight to Viking 1 pressure data, thus rejecting the idea of a monotonic SPRC
685　mass balance over the years. The possibility of an erosion of the SPRC following the storm
686　in MY 34 is difficult to show from the pressure data. First, the pressure recorded by MSL
687　at the end of MY 34 was strongly impacted by a local dust storm (Viúdez-Moreiras et
688　al., 2020). Moreover, when the storm stopped, the northern seasonal cap was still form-
689　ing, with potentially an anomalous extent that lead to a decrease in the available atmo-
690　spheric mass (de la Torre Juarez et al., 2019). The uncertainty in both the data and the
691　interpolation, represented by the error bars in Figure 9, also explain the deficit observed
692　by InSight and MSL. These two comparisons suggest again that there is no significant
693　long-term pressure change.

694　## 5.2 CO_2 cycle and dust

695　　　　What can induce year-to-year variations in the seasonal CO_2 ice budget? As re-
696　viewed in Titus et al. (2017), the CO_2 ice condensation and sublimation rates are con-
697　trolled by the local energy balance, as the CO_2 condenses or sublimes in the exact amount
698　needed to keep the surface and atmosphere at the CO_2 condensation temperature when
699　ice is present.

700　　　　At a given season, this energy balance could fluctuate from one year to the other.
701　This stems from interannual changes in both CO_2 ice albedo and emissivity, as well as
702　changes in the incident infrared radiation due to variations in the heat advected by the
703　atmosphere or by the clouds. It is also sensitive to the amount of heat stored in the sub-
704　surface during previous seasons: the heat conducted from the subsurface up to the CO_2
705　ice on the surface depends on the subsurface temperatures, which are themselves influ-
706　enced by the temperature from the previous summer when no CO_2 ice was present.

707　　　　On these grounds, atmospheric dust can influence the CO_2 budget in a variety of
708　ways:

709　　　　Firstly, during the condensation phase (i.e. in the polar night), dust primarily in-
710　creases the thermal emissivity of the atmosphere and thus its radiative cooling (Pollack
711　et al., 1990). More CO_2 condenses in the atmosphere and less on the surface. The net
712　effect is an observed decrease of the thermal infrared emission at the top of the atmo-
713　sphere due to the radiative effect of CO_2 clouds and/or the lower emissivity of the CO_2
714　snow freshly deposited from the atmosphere (Forget & Pollack, 1996; Cornwall & Titus,
715　2009). This means less CO_2 ice condensing during a dust storm reaching the polar night.
716　CO_2 ice deposits that condensed in the presence of extra dust may also be durably mod-
717　ified. They could have a higher albedo because they were formed from larger fractions
718　of small particles condensed in the atmosphere, but their albedo could also be lowered
719　by the contamination of more dust particles. Which effects dominate? Looking at the
720　seasonal deposits around the north pole, Byrne et al. (2008) found that the northern fall
721　2001 global dust-storm resulted in slightly brighter ice deposits in the following spring.
722　They considered this result to be "counter-intuitive". It can probably be attributed to
723　comparatively more atmospheric condensation in fall enhancing the spring albedo. The
724　amount of airborne dust also influences the atmospheric circulation and thus the trans-
725　port of heat and the dilution of non-condensable gas. The concentration of these gases
726　influences the CO_2 condensation temperature (Forget et al., 2008; Piqueux et al., 2020).

727   Secondly, during the sublimation phase, or more generally when CO_2 ice is signif-
728 icantly sunlit, the net effect of airborne dust is also equivocal, as studied by Bonev (2002);
729 Bonev et al. (2008). Airborne dust redistributes the downward radiation from solar to
730 thermal infrared because dust absorbs solar radiations and re-emit at thermal wavelengths.
731 Model calculation and camera observations show that regions of high-albedo CO_2 frost
732 will sublimate faster with more airborne dust (as they mostly absorb in the thermal range)
733 whereas low-albedo regions will sublimate slower (as they mostly absorb in the visible)
734 (Bonev et al., 2003; Bonev et al., 2008).

735   Thirdly, during summer (when no CO_2 ice is present) airborne dust could also mod-
736 ify the mean surface temperature at high latitude and the stored subsurface heat, but
737 once again the net effect is subtle and depends on the atmospheric temperatures and sur-
738 face albedo.

739   Overall, determining the net effect of regional and global dust storms on the sea-
740 sonal CO_2 cycle is not straightforward as the different processes involved could tend to
741 balance each other. This may explains why the seasonal cycle was observed to be rel-
742 atively insensitive to the occurrence or non-occurrence of global dust storms in the multi-
743 year Viking Lander pressure records (James et al., 1992). Now the InSight pressure mea-
744 surements suggest that the Northern seasonal polar cap was slightly and unusually more
745 massive during the winter and spring of MY 34 (after $L_s=300°$) following an unusual global
746 dust storm that occurred throughout the preceding autumn, well before the observed ef-
747 fect on the seasonal ice cap, in accordance with the observations from MSL de la Torre Juarez
748 et al. (2019). Based on the discussion above, we can speculate that the most likely rea-
749 son for this small excess of mass could be due to a slight increase of the ice albedo, re-
750 sulting from more atmospheric condensation during fall. An alternative explanation could
751 invoke the fact that the post-storm winter atmosphere in the polar night could be slightly
752 depleted in airborne dust and/or ice clouds compared to regular years, reducing the frac-
753 tion of CO_2 ice clouds and snowfall and therefore increasing the polar night thermal in-
754 frared cooling to space, and thus the net condensation rate.

755   In theory, these hypotheses could be tested using climate simulations performed
756 with a GCM. The current version of the LMD GCM can account for the effect of dust
757 on the atmospheric dynamics and radiative cooling as well as their consequence on the
758 atmospheric CO_2 condensation and its effect on the polar night emissivity (Forget et al.,
759 1998). However, because of the lack of dust observations in the polar night, the dust cli-
760 matology available to simulate MY 34 (Montabone et al., 2020) in the polar regions is
761 probably not adequate to represent well what happened (either during or after the dust
762 storm). Furthermore, the GCM does not include any feedback on the CO_2 ice deposit
763 albedo, which cannot be affected by the effect of a dust storm (neither the albedo increase
764 due to the additional atmospheric condensation or decrease by the additional dust con-
765 tamination). Nevertheless, we performed GCM simulations using the MY 34 and MY 35
766 dust scenarios (Montabone et al., 2015), looking for other differences that could result
767 from the MY 34 global dust storm. The simulated CO_2 mass cycles in the two years were
768 found to be almost almost identical (not shown), confirming that processes that are well
769 represented in the GCM (e.g. atmospheric dynamic and heat transport, non-condensible
770 gas enrichment) are probably not involved in the interannual seasonal cap variations ob-
771 served by InSight.

6 Conclusions

773   In this study, we compare for the first time the InSight pressure sensor data with
774 Viking data taken 40 years earlier, to detect long-term pressure changes, and with other
775 available surface pressure records. The main conclusions of this investigation are:

- InSight pressure measurements have an unexpected thermal sensitivity to sensor temperature, which dramatically impacts the recorded annual pressure and makes its evolution inconsistent over the two years of the mission.
- A polynomial correction in the sensor temperature is proposed, using a ratio of MSL pressure data to account for the interannual variability of the seasonal pressure cycle, observed by MSL between the beginning of MY 34 and 35.
- InSight data, once recalibrated, have an uncertainty of 1.7 to 2.3 Pa at 1-σ compared to the initial uncertainty of 1.5 Pa at 1-σ. The correction does not lead to a major uncertainty compromising the detection of secular pressure changes compared to the Viking data, or of interannual changes.
- The comparison between MSL and InSight pressure during MY 34 and 35 reinforces the credibility of our correction. This comparison also highlights a pressure deficit at the MSL site at $L_s \sim 270°$. This deficit could be induced by a change in the scale height due to a significant amount of dust within Gale Crater, creating a hot atmospheric layer in the local near-surface atmosphere.
- We design two high-accuracy methods for pressure interpolation, at local and global scales, that correct the effects of local and large-scale atmospheric circulations as well as the Martian orography on the seasonal pressure variations. Both methods use a scale height computed with the air temperature at an altitude of 1 km. The influence of atmospheric parameters on this interpolation was quantified at 1% of the absolute pressure at a 3-σ level.
- The Viking 1 and InSight pressure comparison does not show significant secular pressure change, as previously postulated with the Viking and Phoenix comparison. This suggests that either the sublimation of the SPRC is much slower than expected, or that the system is actually in equilibrium. In any case, it appears that the mass balance computations that predicted a very large increase in atmospheric mass or the rapid SPRC disappearance are overestimated.
- Similarly, a visual comparative analysis of Viking 2 orbiter and MARCI images of the seasonal ice caps does not show significant change in the dynamics of the seasonal ice caps, as observed when comparing the annual variations of the ice caps with pressure data.
- Both of these conclusions are also supported by the comparison between MSL and Viking 1 pressure data. Using the five martian years of MSL pressure records, we cannot establish a secular trend.
- Phoenix surface pressure data might highlight an increase of the atmospheric mass during MY 29, suggesting a possible erosion of the SPRC after the MY 28 global dust storm. Analysis of the SPRC boundary during MY 27, 28, and 29 would help to study this assumption.
- The NSPC is more extended during MY 34 compared to MY 35. However, the physical mechanisms that explain this extent are not understood yet. Investigations conducted with the LMD GCM suggest that atmospheric dynamics, heat transport, or non-condensible gas enrichment are not at the origin of this phenomenon.

The Perseverance rover that arrived on Mars on February 18th, 2021 at a latitude close to Viking 1 lander will provide a unique new pressure dataset to contribute to the study of interannual and secular pressure changes. Cross-analyses between SPRC evolution, dust storms, and atmospheric mass measurements would also help to better understand the evolution of the SPRC and its relative balance.

Appendix A Impact of MSL pressure uncertainties on InSight pressure correction

We apply the propagation of uncertainty on the definition of β (Eq. 6):

$$\frac{\sigma_\beta}{\beta} = \sqrt{\left(\frac{\sigma_{P_{\mathrm{MSL,Yr\ 1}}}}{P_{\mathrm{MSL,Yr\ 1}}}\right)^2 + \left(\frac{\sigma_{P_{\mathrm{MSL,Yr\ 2}}}}{P_{\mathrm{MSL,Yr\ 2}}}\right)^2 - 2\frac{Cov(P_{\mathrm{MSL,Yr\ 1}}, P_{\mathrm{MSL,Yr\ 2}})}{P_{\mathrm{MSL,Yr\ 1}}P_{\mathrm{MSL,Yr\ 2}}}} \tag{A1}$$

826   where $Cov(P_{\mathrm{MSL,Yr\ 1}}, P_{\mathrm{MSL,Yr\ 2}})$ is the covariance between measurements $P_{\mathrm{MSL,Yr\ 1}}$
827 and $P_{\mathrm{MSL,Yr\ 2}}$.

828   Let us assume that:

$$P_{\mathrm{MSL,Yr\ 1}} = P_{\mathrm{MSL}}(t_{Yr1}) = P_{\mathrm{atm,true}}(t_{Yr1}) + \epsilon(t_{Yr1}) + \delta(t_{Yr1}) \tag{A2}$$

$$P_{\mathrm{MSL,Yr\ 2}} = P_{\mathrm{MSL}}(t_{Yr2}) = P_{\mathrm{atm,true}}(t_{Yr2}) + \epsilon(t_{Yr2}) + \delta(t_{Yr2}) \tag{A3}$$

829   with

830 • $P_{\mathrm{atm,\ true}}(t)$ the true atmospheric pressure that MSL should have recorded with-
831   out any error
832 • $\epsilon(t)$ the error on a measurement due to:

833   – The error on the absolute measurement due to the initial calibration, estimated
834   to be at most 4 Pa at 3-σ over the possible pressure range at the MSL landing
835   site (Harri et al., 2014).
836   – The error due to elevation change. During the period considered here, the al-
837   titude of the rover changed by nearly 100 m, which could lead to a change in
838   pressure of 8 Pa at 3-σ .
839   – At least, the estimated error is $\sqrt{8^2 + 4^2} \approx 9$ Pa at 3-σ
840   – Since 15-day averaged data are used, the uncertainty related to the precision
841   of the measurements is assumed to be negligible.

842 • $\delta(t)$, the drift error which theoretically evolves at a rate of 1 Pa/Martian year at
843   3-σ (Harri et al., 2014).

844   We model these errors by random variables whose variance is given by the previ-
845 ous values. The last two terms in the expression of P_{MSL}, thus representing the error on
846 the measurement, are random variables of variance. We introduce $\sigma_{P_{\mathrm{MSL}}} = \sqrt{\sigma_\epsilon^2 + \sigma_\delta^2}$
847 by independence of these two terms.

848   Since the errors are computed over the range of possible values of the MSL mea-
849 surements and not a precise value, the errors ϵ, δ are independent of $P_{\mathrm{atm,true}}$. Moreover,
850 the $P_{\mathrm{atm,true}}$ between the two years are completely independent. Using the bilinearity
851 of the covariance, and these independences, we obtain:

$$Cov(P_{\mathrm{MSL},Yr1}, P_{MSL,Yr2}) = Cov(\epsilon(t_{Yr1}), \epsilon(t_{Yr2})) + Cov(\delta(t_{Yr1}), \delta(t_{Yr2})) \tag{A4}$$

852   By definition, for two random variables a, b:

$$Cov(a, b) = \rho(a, b)\sigma_a\sigma_b \tag{A5}$$

853   with ρ the correlation coefficient. ϵ has been determined during calibration tests
854 and is assumed to be constant over the mission, so that

$$Cov(\epsilon(t_{Yr1}), \epsilon(t_{Yr2})) = \sigma_\epsilon^2 \tag{A6}$$

855   Assuming that the drift grows at a rate of 1 Pa/MY, we have:

$$Cov(\delta(t_{Yr1}), \delta(t_{Yr2})) = Cov(\delta(t_{Yr1}), \delta(t_{Yr1}) + 1) = Cov(\delta(t_{Yr1}), \delta(t_{Yr1})) \quad \text{(A7)}$$

by property of the covariance. We thus have:

$$Cov(\delta(t_{Yr1}), \delta(t_{Yr2})) = \sigma_\delta^2 \quad \text{(A8)}$$

856   Hence, Eq. A4 becomes:

$$\frac{\sigma_\beta}{\beta} = \sigma_{P_{\text{MSL}}} \sqrt{\left(\frac{1}{P_{\text{MSL},Yr1}} - \frac{1}{P_{\text{MSL},Yr2}} \right)^2} \quad \text{(A9)}$$

which gives:

$$\frac{\sigma_\beta}{\beta} \sim 5 \times 10^{-5} \quad \text{(A10)}$$

Open Research

858   InSight pressure uncorrected data can be retrieved on the PDS at `https://atmos`
859   `.nmsu.edu/PDS/data/PDS4/InSight/ps_bundle/data_calibrated/` (Banfield, 2019)
860   , MSL REMS data at `https://atmos.nmsu.edu/PDS/data/mslrem_1001/DATA/` (Gomez-
861   Elvira, 2013), Viking 1 at `https://nssdc.gsfc.nasa.gov/nmc/dataset/display.action`
862   `?id=PSPA-00526` (Tillman, 1989). Phoenix corrected data are given with Taylor et al.
863   (2010). Marci mosaics can be reconstructed from the images that are available at `https://`
864   `pds-imaging.jpl.nasa.gov/data/mro/mars_reconnaissance_orbiter/marci/mrom`
865   `_0867/data/` for Fig. 8b and `https://pds-imaging.jpl.nasa.gov/data/mro/mars_reconnaissance`
866   `_orbiter/marci/mrom_1197/data/` for Fig. 8c (Malin et al., 2001). The two THEMIS
867   VIS images are available from the THEMIS Data Node under the Planetary Data Sys-
868   tem (`https://viewer.mars.asu.edu/viewer/themis#P=V65575024&T=2`; `https://viewer`
869   `.mars.asu.edu/viewer/themis#P=V63417011&T=2`) (Christensen et al., 2002). The Mars
870   Climate Database can be retrieved upon request (see `http://www-mars.lmd.jussieu`
871   `.fr/mars/access.html`).

872   Data files for figures used in this analysis are available in a public repository, see
873   Lange et al. (2022).

References

Banerdt, W. B., Smrekar, S. E., Banfield, D., Giardini, D., Golombek, M., Johnson, C. L., ... Wieczorek, M. (2020). Initial results from the insight mission on mars. *Nature Geoscience*, *13*(3), 183-189. doi: 10.1038/s41561-020-0544-y

Banfield, D. (2019). Insight apss ps data product bundle.

Banfield, D., Rodriguez-Manfredi, J. A., Russell, C. T., Rowe, K. M., Leneman, D., Lai, H. R., . . . Team, T. T. (2019). Insight auxiliary payload sensor suite (apss). *Space Science Reviews*, *215*(1), 4. doi: 10.1007/s11214-018-0570-x

Banfield, D., Spiga, A., Newman, C., Forget, F., Lemmon, M., Lorenz, R., . . . Banerdt, W. B. (2020). The atmosphere of mars as observed by insight. *Nature Geoscience*, *13*(3), 190-198. doi: 10.1038/s41561-020-0534-0

Barnes, J. R. (1980). Time spectral analysis of midlatitude disturbances in the martian atmosphere. *Journal of Atmospheric Sciences*, *37*(9), 2002 - 2015. doi: 10.1175/1520-0469(1980)037<2002:TSAOMD>2.0.CO;2

Becerra, P., Byrne, S., & Brown, A. J. (2015). Transient bright "halos" on the south polar residual cap of mars: Implications for mass-balance. *Icarus*, *251*, 211–225. doi: 10.1016/j.icarus.2014.04.050

Blackburn, D. G., Bryson, K. L., Chevrier, V. F., Roe, L. A., & White, K. F. (2010). Sublimation kinetics of co2 ice on mars. *Planetary and Space Science*, *58*(5), 780-791. doi: 10.1016/j.pss.2009.12.004

Bonev, B. P. (2002). Regression of the mountains of mitchel polar ice after the onset of a global dust storm on mars. *Geophysical Research Letters*, *29*(21). doi: 10.1029/2002gl015458

Bonev, B. P., Hansen, G. B., Glenar, D. A., James, P. B., & Bjorkman, J. E. (2008). Albedo models for the residual south polar cap on mars: Implications for the stability of the cap under near-perihelion global dust storm conditions. *Planetary and Space Science*, *56*(2), 181-193. (Mars Polar Processes: Atmosphere-Surface Interactions) doi: 10.1016/j.pss.2007.08.003

Bonev, B. P., James, P. B., Bjorkman, J. E., Hansen, G. B., & Wolff, M. J. (2003). Effects of Atmospheric and Surface Dust on the Sublimation Rates of CO2 on Mars. In S. Clifford, P. Doran, D. Fisher, & C. Herd (Eds.), *Third international conference on mars polar science and exploration* (p. 8052).

Buhler, P. B., Ingersoll, A. P., Piqueux, S., Ehlmann, B. L., & Hayne, P. O. (2020). Coevolution of mars's atmosphere and massive south polar CO2 ice deposit. , *4*(4), 364–371. doi: 10.1038/s41550-019-0976-8

Byrne, S., Hayne, P. O., Becerra, P., & HiRISE Team. (2015). Evolution and Stability of the Residual CO2 Ice Cap. In *Lunar and planetary science conference* (p. 1657).

Byrne, S., Zuber, M. T., & Neumann, G. A. (2008). Interannual and seasonal behavior of Martian residual ice-cap albedo. , *56*(2), 194-211. doi: 10.1016/j.pss.2006.03.018

Calvin, W., Cantor, B., & James, P. (2017). Interannual and seasonal changes in the south seasonal polar cap of mars: Observations from my 28-31 using marci. *Icarus*, *292*, 144-153. doi: 10.1016/j.icarus.2017.01.010

Calvin, W., James, P., Cantor, B., & Dixon, E. (2015). Interannual and seasonal changes in the north polar ice deposits of mars: Observations from my 29–31 using marci. *Icarus*, *251*, 181-190. (Dynamic Mars) doi: 10.1016/j.icarus.2014.08.026

Chatain, A., Spiga, A., Banfield, D., Forget, F., & Murdoch, N. (2021). Seasonal variability of the daytime and nighttime atmospheric turbulence experienced by insight on mars. *Geophysical Research Letters*, *48*(22), e2021GL095453. (e2021GL095453 2021GL095453) doi: 10.1029/2021GL095453

Christensen, P., Gorelick, N., Mehall, G., & Murray, K. (2002). 2001 mars odyssey thermal emission imaging system visible geometrically registered data product.

Christensen, P. R., Jakosky, B. M., Kieffer, H. H., Malin, M. C., Harry Y. McSween, J., Nealson, K., . . . Ravine, M. (2004). The thermal emission imaging system (THEMIS) for the mars 2001 odyssey mission. *Space Science Reviews*, *110*(1/2), 85–130. doi: 10.1023/b:spac.0000021008.16305.94

Cornwall, C., & Titus, T. N. (2009). Spatial and temporal distributions of martian north polar cold spots before, during, and after the global dust storm of 2001. *Journal of Geophysical Research*, *114*(E2). doi: 10.1029/2008je003243

de la Torre Juarez, M., Piqueux, S., Kass, D. M., Newman, C., & Guzewich, S. D. (2019). Pressure deficit in gale crater and a larger northern polar cap after the mars year 34 global dust storm. In *Agu fall meeting abstracts* (Vol. 2019, p. P51C-02).

Fonseca, R. M., Zorzano-Mier, M.-P., & Martín-Torres, J. (2018). Planetary boundary layer and circulation dynamics at gale crater, mars. *Icarus*, *302*, 537-559. doi: 10.1016/j.icarus.2017.11.036

Forget, F., Hourdin, F., Fournier, R., Hourdin, C., Talagrand, O., Collins, M., . . . Huot, J.-P. (1999). Improved general circulation models of the martian atmosphere from the surface to above 80 km. *Journal of Geophysical Research: Planets*, *104*(E10), 24155-24175. doi: 10.1029/1999JE001025

Forget, F., Hourdin, F., & Talagrand, O. (1998). Co2snowfall on mars: Simulation with a general circulation model. *Icarus*, *131*(2), 302-316. doi: 10.1006/icar .1997.5874

Forget, F., Millour, E., Montabone, L., & Lefevre, F. (2008). Non Condensable Gas Enrichment and Depletion in the Martian Polar Regions. In *Third international workshop on the mars atmosphere: Modeling and observations* (Vol. 1447, p. 9106).

Forget, F., & Pollack, J. B. (1996). Thermal infrared observations of the condensing martian polar caps: CO2ice temperatures and radiative budget. *Journal of Geophysical Research: Planets*, *101*(E7), 16865–16879. doi: 10.1029/96je01077

Forget, F., Spiga, A., Dolla, B., Vinatier, S., Melchiorri, R., Drossart, P., . . . Gondet, B. (2007). Remote sensing of surface pressure on mars with the mars express/omega spectrometer: 1. retrieval method. *Journal of Geophysical Research: Planets*, *112*(E8). doi: 10.1029/2006JE002871

Golombek, M., Williams, N., Warner, N. H., Parker, T., Williams, M. G., Daubar, I., . . . Sklyanskiy, E. (2020). Location and setting of the mars insight lander, instruments, and landing site. *Earth and Space Science*, *7*(10), e2020EA001248. doi: 10.1029/2020EA001248

Gomez-Elvira, J. (2013). Mars science laboratory rover environmental monitoring station rdr data v1.0.

Gómez-Elvira, J., Armiens, C., Carrasco, I., Genzer, M., Gómez, F., Haberle, R., . . . Zorzano, M.-P. (2014). Curiosity's rover environmental monitoring station: Overview of the first 100 sols. *Journal of Geophysical Research: Planets*, *119*(7), 1680-1688. doi: 10.1002/2013JE004576

Haberle, R. M., Gómez-Elvira, J., de la Torre Juárez, M., Harri, A.-M., Hollingsworth, J. L., Kahanpää, H., . . . Teams, R. S. (2014). Preliminary interpretation of the rems pressure data from the first 100 sols of the msl mission. *Journal of Geophysical Research: Planets*, *119*(3), 440-453. doi: 10.1002/2013JE004488

Haberle, R. M., & Kahre, M. A. (2010). Detecting secular climate change on Mars. *International Journal of Mars Science and Exploration*, *4*, 68-75. doi: 10.1555/ mars.2010.0003

Harri, A. M., Genzer, M., Kemppinen, O., Kahanpää, H., Gomez-Elvira, J., Rodriguez-Manfredi, J. A., . . . REMS/MSL Science Team (2014). Pressure observations by the Curiosity rover: Initial results. *Journal of Geophysical Research (Planets)*, *119*(1), 82-92. doi: 10.1002/2013JE004423

Hess, S. L., Henry, R. M., Leovy, C. B., Ryan, J. A., Tillman, J. E., Chamberlain, T. E., . . . Mitchell, J. L. (1976). Preliminary meterological results on mars from the viking 1 lander. *Science*, *193*(4255), 788-791.

Hess, S. L., Ryan, J. A., Tillman, J. E., Henry, R. M., & Leovy, C. B. (1980). The

annual cycle of pressure on mars measured by viking landers 1 and 2. *Geophysical Research Letters*, *7*, 197-200.

Holstein-Rathlou, C., Gunnlaugsson, H., Cantor, B., Ellehøj, M., Lange, C., Lemmon, M., ... Smith, P. (2010). On dust storms observed at the phoenix landing site.. (Conference date: 01-03-2010 Through 05-03-2010)

Hourdin, F., Forget, F., & Talagrand, O. (1995). The sensitivity of the martian surface pressure and atmospheric mass budget to various parameters: A comparison between numerical simulations and viking observations. *Journal of Geophysical Research: Planets*, *100*(E3), 5501-5523. doi: 10.1029/94JE03079

Hourdin, F., Van, P. L., Forget, F., & Talagrand, O. (1993). Meteorological variability and the annual surface pressure cycle on mars. *Journal of Atmospheric Sciences*, *50*(21), 3625 - 3640. doi: 10.1175/1520-0469(1993)050<3625:MVATAS>2.0.CO;2

James, P., Thomas, P., & Malin, M. (2010). Variability of the south polar cap of mars in mars years 28 and 29. *Icarus*, *208*(1), 82–85. doi: 10.1016/j.icarus.2010.02.007

James, P. B. (1979). Recession of martian north polar cap: 1977–1978 viking observations. *Journal of Geophysical Research*, *84*(B14), 8332. doi: 10.1029/jb084ib14p08332

James, P. B. (1982). Recession of martian north polar cap: 1979–1980 viking observations. *Icarus*, *52*(3), 565–569. doi: 10.1016/0019-1035(82)90016-1

James, P. B., Briggs, G., Barnes, J., & Spruck, A. (1979). Seasonal recession of mars' south polar cap as seen by viking. *Journal of Geophysical Research*, *84*(B6), 2889. doi: 10.1029/jb084ib06p02889

James, P. B., Kieffer, H. H., & Paige, D. A. (1992). The seasonal cycle of carbon dioxide on Mars. In M. George (Ed.), *Mars* (p. 934-968).

James, P. B., & Lumme, K. (1982). Martian south polar cap boundary: 1971 and 1973 data. *Icarus*, *50*(2-3), 368–380. doi: 10.1016/0019-1035(82)90130-0

James, P. B., Malolepszy, K. M., & Martin, L. J. (1987). Interannual variability of mars' south polar cap. *Icarus*, *71*(2), 298–305. doi: 10.1016/0019-1035(87)90154-0

Kahanpää, H., Polkko, J., & Daly, M. (2021). Accuracy of the phoenix and viking atmospheric pressure measurements: impact on detecting the climate change on mars. doi: 10.5194/epsc2021-63

Kahanpää, H., Newman, C., Moores, J., Zorzano, M.-P., Martín-Torres, J., Navarro, S., ... Schmidt, W. (2016). Convective vortices and dust devils at the msl landing site: Annual variability. *Journal of Geophysical Research: Planets*, *121*(8), 1514-1549. doi: 10.1002/2016JE005027

Kahre, M. A., & Haberle, R. M. (2010). Mars co2 cycle: Effects of airborne dust and polar cap ice emissivity. *Icarus*, *207*(2), 648-653. doi: 10.1016/j.icarus.2009.12.016

Kieffer, H. H., Neugebauer, G., Munch, G., Chase, S. C., & Miner, E. (1972). Infrared thermal mapping experiment: The viking mars orbiter. *Icarus*, *16*(1), 47-56.

Lange, L., F.Forget, D.Banfield, M.Wolff, A.Spiga, E.Millour, ... W.B.Banerdt (2022). *InSight Pressure Data Recalibration, and its Application to the Study of Long-Term Pressure Changes on Mars.* Harvard Dataverse. Retrieved from https://doi.org/10.7910/DVN/RUWICY doi: 10.7910/DVN/RUWICY

Langevin, Y., Bibring, J.-P., Montmessin, F., Forget, F., Vincendon, M., Douté, S., ... Gondet, B. (2007). Observations of the south seasonal cap of Mars during recession in 2004–2006 by the OMEGA visible/near-infrared imaging spectrometer on board Mars Express. *Journal of Geophysical Research. Planets*, *112*(E8), E08S12. doi: 10.1029/2006JE002841

Leighton, R. B., & Murray, B. C. (1966). Behavior of carbon dioxide and other volatiles on mars. *Science*, *153*(3732), 136–144. doi: 10.1126/science.153.3732 .136

Malin, M. C., Bell III, J. F., Calvin, W., Clancy, R. T., Haberle, R. M., James, P. B., . . . Caplinger, M. A. (2001). Mars color imager (marci) on the mars climate orbiter. *Journal of Geophysical Research E: Planets*, *106*(E8), 17651-17672.

Malin, M. C., Caplinger, M. A., & Davis, S. D. (2001). Observational evidence for an active surface reservoir of solid carbon dioxide on mars. *Science*, *294*(5549), 2146–2148. doi: 10.1126/science.1066416

Martínez, G. M., Newman, C. N., De Vicente-Retortillo, A., Fischer, E., Renno, N. O., Richardson, M. I., . . . Vasavada, A. R. (2017). The Modern Near-Surface Martian Climate: A Review of In-situ Meteorological Data from Viking to Curiosity. , *212*(1-2), 295-338. doi: 10.1007/s11214-017-0360-x

Martínez, G., Fischer, E., Rennó, N., Sebastián, E., Kemppinen, O., Bridges, N., . . . Gómez-Elvira, J. (2016). Likely frost events at gale crater: Analysis from msl/rems measurements. *Icarus*, *280*, 93-102. (MicroMars to MegaMars) doi: 10.1016/j.icarus.2015.12.004

McCleese, D. J., Schofield, J. T., Taylor, F. W., Calcutt, S. B., Foote, M. C., Kass, D. M., . . . Zurek, R. W. (2007). Mars climate sounder: An investigation of thermal and water vapor structure, dust and condensate distributions in the atmosphere, and energy balance of the polar regions. *Journal of Geophysical Research: Planets*, *112*(E5). doi: 10.1029/2006JE002790

Millour, E., Forget, F., Spiga, A., Vals, M., Zakharov, V., Montabone, L., . . . MCD Development Team (2018). The Mars Climate Database (version 5.3). In *From mars express to exomars* (p. 68).

Mitchell, M. (1977). Evaluation of viking lander barometric pressure sensor.

Montabone, L., Forget, F., Millour, E., Wilson, R., Lewis, S., Cantor, B., . . . Wolff, M. (2015). Eight-year climatology of dust optical depth on mars. *Icarus*, *251*, 65-95. (Dynamic Mars) doi: 10.1016/j.icarus.2014.12.034

Montabone, L., Spiga, A., Kass, D. M., Kleinböhl, A., Forget, F., & Millour, E. (2020). Martian year 34 column dust climatology from mars climate sounder observations: Reconstructed maps and model simulations. *Journal of Geophysical Research: Planets*, *125*(8), e2019JE006111. doi: 10.1029/2019JE006111

Moore, C. A., Moores, J. E., Newman, C. E., Lemmon, M. T., Guzewich, S. D., & Battalio, M. (2019). Vertical and horizontal heterogeneity of atmospheric dust loading in northern gale crater, mars. *Icarus*, *329*, 197-206. doi: 10.1016/j.icarus.2019.03.041

Morris, E. C., & Jones, K. L. (1980). Viking 1 lander on the surface of mars: Revised location. *Icarus*, *44*(1), 217-222.

Newman, C. E., Kahanpää, H., Richardson, M. I., Martínez, G. M., Vicente-Retortillo, A., & Lemmon, M. T. (2019). Marswrf convective vortex and dust devil predictions for gale crater over 3 mars years and comparison with msl-rems observations. *Journal of Geophysical Research: Planets*, *124*(12), 3442-3468. doi: 10.1029/2019JE006082

Ordonez-Etxeberria, I., Hueso, R., & Sánchez-Lavega, A. (2018, January). A systematic search of sudden pressure drops on Gale crater during two Martian years derived from MSL/REMS data. , *299*, 308-330. doi: 10.1016/j.icarus.2017.07.032

Ordonez-Etxeberria, I., Hueso, R., Sánchez-Lavega, A., Millour, E., & Forget, F. (2019). Meteorological pressure at gale crater from a comparison of rems/msl data and mcd modelling: Effect of dust storms. *Icarus*, *317*, 591-609. doi: 10.1016/j.icarus.2018.09.003

Piqueux, S., & Christensen, P. R. (2008). Deposition of co2 and erosion of the martian south perennial cap between 1972 and 2004: Implications for current

climate change.   *Journal of Geophysical Research: Planets*, *113*(E2).   doi: 10.1029/2007JE002969

Piqueux, S., Kleinböhl, A., Hayne, P. O., Kass, D. M., Heavens, N., McCleese, D. J., ... Shirley, J. (2020). Atmospheric CO2 Depletion at the Surface in the Polar Regions of Mars.   In *Seventh international conference on mars polar science and exploration* (Vol. 2099, p. 6016).

Piqueux, S., Kleinböhl, A., Hayne, P. O., Kass, D. M., Schofield, J. T., & Mc-Cleese, D. J.   (2015).   Variability of the martian seasonal co2 cap extent over eight mars years.   *Icarus*, *251*, 164-180.   (Dynamic Mars)   doi: 10.1016/j.icarus.2014.10.045

Pla-Garcia, J., Rafkin, S. C., Kahre, M., Gomez-Elvira, J., Hamilton, V. E., Navarro, S., ... R. Vasavada, A.   (2016).   The meteorology of gale crater as determined from rover environmental monitoring station observations and numerical modeling. part i: Comparison of model simulations with observations.   *Icarus*, *280*, 103-113.   (MicroMars to MegaMars)   doi: 10.1016/j.icarus.2016.03.013

Pollack, J. B., Haberle, R. M., Schaeffer, J., & Lee, H.   (1990).   Simulations of the general circulation of the martian atmosphere: 1. polar processes.   *Journal of Geophysical Research*, *95*(B2), 1447. doi: 10.1029/jb095ib02p01447

Press, W. H., Teukolsky, S. A., Vetterling, W. T., & Flannery, B. P.   (1993).   *Numerical recipes in fortran; the art of scientific computing* (2nd ed.).   USA: Cambridge University Press.

Rafkin, S. C., Pla-Garcia, J., Kahre, M., Gomez-Elvira, J., Hamilton, V. E., Marín, M., ... Vasavada, A.   (2016).   The meteorology of gale crater as determined from rover environmental monitoring station observations and numerical modeling. part ii: Interpretation. *Icarus*, *280*, 114-138. (MicroMars to MegaMars) doi: 10.1016/j.icarus.2016.01.031

Rangarajan, V. G., & Ghosh, M. (2020). Seasonal thermal inertia variations at gale crater: Role of active surface deposition phenomena. *Icarus*, *337*, 113499. doi: 10.1016/j.icarus.2019.113499

Richardson, M. I., & Newman, C. E.   (2018).   On the relationship between surface pressure, terrain elevation, and air temperature. part i: The large diurnal surface pressure range at gale crater, mars and its origin due to lateral hydrostatic adjustment.   *Planetary and Space Science*, *164*, 132-157.   doi: 10.1016/j.pss.2018.07.003

Ryan, J. A., & Sharman, R. D.   (1981).   Two major dust storms, one mars year apart: Comparison from viking data.   *Journal of Geophysical Research: Oceans*, *86*(C4), 3247-3254. doi: 10.1029/JC086iC04p03247

Seiff, A. (1976). The viking atmosphere structure experiment - techniques, instruments, and expected accuracies. *Space Science Instrumentation*, *2*, 381-423.

Seiff, A., & Kirk, D. B.   (1977).   Structure of the atmosphere of mars in summer at mid-latitudes. *Journal of Geophysical Research*, *82*, 4364-4378. doi: 10.1029/JS082i028p04364

Spiga, A., Banfield, D., Teanby, N. A., Forget, F., Lucas, A., Kenda, B., ... Banerdt, W. B.   (2018).   Atmospheric science with insight.   *Space Science Reviews*, *214*(7), 109. doi: 10.1007/s11214-018-0543-0

Spiga, A., & Forget, F.   (2009).   A new model to simulate the martian mesoscale and microscale atmospheric circulation: Validation and first results. *Journal of Geophysical Research: Planets*, *114*(E2). doi: 10.1029/2008JE003242

Spiga, A., Forget, F., Dolla, B., Vinatier, S., Melchiorri, R., Drossart, P., ... Gondet, B. (2007). Remote sensing of surface pressure on mars with the mars express/omega spectrometer: 2. meteorological maps.   *Journal of Geophysical Research: Planets*, *112*(E8). doi: 10.1029/2006JE002870

Spiga, A., Murdoch, N., Lorenz, R., Forget, F., Newman, C., Rodriguez, S., ... Banerdt, W. B.   (2021).   A study of daytime convective vortices and turbu-

lence in the martian planetary boundary layer based on half-a-year of insight atmospheric measurements and large-eddy simulations. *Journal of Geophysical Research: Planets*, *126*(1), e2020JE006511. doi: 10.1029/2020JE006511

Steakley, K., & Murphy, J. (2016). A year of convective vortex activity at gale crater. *Icarus*, *278*, 180-193. doi: 10.1016/j.icarus.2016.06.010

Taylor, P. A., Kahanpää, H., Weng, W., Akingunola, A., Cook, C., Daly, M., . . . Whiteway, J. (2010). On pressure measurement and seasonal pressure variations during the phoenix mission. *Journal of Geophysical Research: Planets*, *115*(E3). doi: 10.1029/2009JE003422

Thomas, P., Calvin, W., Cantor, B., Haberle, R., James, P., & Lee, S. (2016). Mass balance of mars' residual south polar cap from ctx images and other data. *Icarus*, *268*, 118-130. doi: 10.1016/j.icarus.2015.12.038

Thomas, P., Calvin, W., Gierasch, P., Haberle, R., James, P., & Sholes, S. (2013). Time scales of erosion and deposition recorded in the residual south polar cap of mars. *Icarus*, *225*(2), 923-932. (Mars Polar Science V) doi: 10.1016/j.icarus.2012.08.038

Thomas, P., James, P., Calvin, W., Haberle, R., & Malin, M. (2009). Residual south polar cap of mars: Stratigraphy, history, and implications of recent changes. *Icarus*, *203*(2), 352-375. doi: 10.1016/j.icarus.2009.05.014

Tillman, J. (1989). Vl1/vl2-m-met-4-daily-avg-pressure-v1.0.

Tillman, J. E. (1988). Mars global atmospheric oscillations: Annually synchronized, transient normal-mode oscillations and the triggering of global dust storms. *Journal of Geophysical Research: Atmospheres*, *93*(D8), 9433-9451. doi: 10.1029/JD093iD08p09433

Tillman, J. E., Johnson, N. C., Guttorp, P., & Percival, D. B. (1993). The martian annual atmospheric pressure cycle: Years without great dust storms. *Journal of Geophysical Research: Planets*, *98*(E6), 10963-10971. doi: 10.1029/93JE01084

Titus, T. N., Byrne, S., Colaprete, A., Forget, F., Michaels, T. I., & Prettyman, T. H. (2017). The co2 cycle. In R. M. Haberle, R. T. Clancy, F. Forget, M. D. Smith, & R. W. Zurek (Eds.), *The atmosphere and climate of mars* (p. 374–404). Cambridge University Press. doi: 10.1017/9781139060172.012

Vicente-Retortillo, Á., Martínez, G. M., Renno, N., Newman, C. E., Ordonez-Etxeberria, I., Lemmon, M. T., . . . Sánchez-Lavega, A. (2018). Seasonal deposition and lifting of dust on mars as observed by the curiosity rover. *Scientific Reports*, *8*(1). doi: 10.1038/s41598-018-35946-8

Viúdez-Moreiras, D., Newman, C. E., de la Torre, M., Martínez, G., Guzewich, S., Lemmon, M., . . . Gómez-Elvira, J. (2019). Effects of the my34/2018 global dust storm as measured by msl rems in gale crater. *Journal of Geophysical Research: Planets*, *124*(7), 1899-1912. doi: 10.1029/2019JE005985

Viúdez-Moreiras, D., Newman, C. E., Forget, F., Lemmon, M., Banfield, D., Spiga, A., . . . and, M. G. (2020). Effects of a large dust storm in the near-surface atmosphere as measured by InSight in elysium planitia, mars. comparison with contemporaneous measurements by mars science laboratory. *Journal of Geophysical Research: Planets*, *125*(9). doi: 10.1029/2020je006493